Neuronal TIMP2 regulates hippocampus-dependent plasticity and extracellular matrix complexity

Ana Catarina Ferreira[1,2,3,4], Brittany M. Hemmer[1,2,3,4,5], Sarah M. Philippi[1,2,3,4,5], Hanxiao Liu[1,2,3,4], Jeffrey D. Zhu[1,2,3,4], Tatyana Kareva[1,2,3,4], Tim Ahfeldt[1,2,3,4], Merina Varghese[1], Patrick R. Hof[1,2], Joseph M. Castellano[1,2,3,4,†]

[1]Nash Family Department of Neuroscience, Friedman Brain Institute, Icahn School of Medicine at Mount Sinai, New York, NY, United States

[2]Ronald M. Loeb Center for Alzheimer's Disease, Icahn School of Medicine at Mount Sinai, New York, NY, United States

[3]Department of Neurology, Icahn School of Medicine at Mount Sinai, New York, NY, United States

[4]Black Family Stem Cell Institute, Icahn School of Medicine at Mount Sinai, New York, NY, United States

[5]Graduate School of Biomedical Sciences, Icahn School of Medicine at Mount Sinai, New York, NY, United States

[†]To whom all correspondence should be addressed

Email: joseph.castellano@mssm.edu

Joseph M. Castellano, Ph.D.

Icahn School of Medicine at Mount Sinai

Nash Family Department of Neuroscience, Department of Neurology

Friedman Brain Institute and Black Family Stem Cell Institute

Ronald M. Loeb Center for Alzheimer’s disease

1425 Madison Ave., Box 1065

New York, NY 10029

Keywords: TIMP2, neurogenesis, synaptic plasticity, memory, extracellular matrix

Abstract

The functional output of the hippocampus, a brain region subserving memory processes, depends on highly orchestrated cellular and molecular processes that regulate synaptic plasticity throughout life. However, little is known regarding the structural requirements of such plasticity and molecular processes involved in this regulation. Specific molecules, including tissue inhibitor of metalloproteinases-2 (TIMP2) have been implicated in serving a pro-plasticity role within the hippocampus, a role that decreases with brain aging. Here, we report that TIMP2 is expressed at high levels in the hippocampus by neurons and its loss in TIMP2 KO mice drives changes in cellular programs related to adult neurogenesis and dendritic spine turnover with corresponding impairments in hippocampus-dependent memory performance. We find that TIMP2 regulates the accumulation of extracellular matrix (ECM) around synapses in the hippocampus with concomitant hindrance in the migration of newborn neurons through a denser ECM network. Deleting the neuronal pool of TIMP2 using a conditional TIMP2 KO mouse reveals that neuronal TIMP2 regulates adult neurogenesis and hippocampus-dependent memory, as well as accumulation of ECM. Our results define a mechanism whereby hippocampus-dependent function is regulated by TIMP2 and its interactions with the ECM to regulate diverse processes associated with synaptic plasticity.

52

53 **Introduction**

54 A variety of cellular, molecular, and functional changes have now been documented in the brain
55 as aging progresses, leaving it susceptible to diseases like Alzheimer's disease. Given that aging
56 serves as the major risk factor for many neurological disorders, aging processes have increasingly
57 been considered to be valid therapeutic targets, especially as the aged population continues to
58 increase. Growing evidence in animal models indicates that the aged brain can be rejuvenated
59 through manipulation of the systemic environment, including through young plasma transfer or
60 sharing of young blood through heterochronic parabiosis (Castellano et al., 2017; Katsimpardi et
61 al., 2014; Villeda et al., 2011; Villeda et al., 2014). Aged mice exposed to young blood exhibit
62 improved synaptic plasticity and cognitive performance (Villeda et al., 2014). We and others have
63 begun to identify factors present in young blood that confer brain rejuvenation phenotypes in aged
64 mice (Castellano et al., 2017; Katsimpardi et al., 2014). Among those, we showed that tissue
65 inhibitor of metalloproteinases-2 (TIMP2), a protein elevated early in life, revitalizes function of
66 the aged mouse hippocampus (Castellano et al., 2017). Despite demonstrating that this factor is
67 critical for young plasma-mediated memory improvements in aged mice (Castellano et al., 2017),
68 little is known of the cellular and molecular details of how TIMP2 regulates function within the
69 hippocampus.

70 TIMP2 is a secreted protein of approximately 21-kDa in size primarily known for its role in
71 regulating peripheral extracellular matrix (ECM) remodeling (Brew and Nagase, 2010) through its
72 unique dual roles in regulating the activation of latent matrix metalloproteinases (MMPs), including
73 MMP2, to proteolytically active forms, and the inhibition of MMP activity (Caterina et al., 2000;
74 Wang et al., 2000). Through these roles, TIMP2 has been shown to play a key role in the
75 maintenance of ECM network structure in many tissues with myriad disease implications,
76 including heart failure (Kandalam et al., 2011), cancer (Kaczorowska et al., 2020), ischemic stroke
77 (Guo et al., 2018), among others. While early reports described expression of TIMP2 from

78 development into adulthood (Fager and Jaworski, 2000), and its role in regulating cortical
79 neuronal differentiation (Perez-Martinez and Jaworski, 2005), and subtle motor phenotypes
80 (Jaworski et al., 2006), few studies have examined the biological role of TIMP2 in the adult brain
81 and how it modulates function of the hippocampus. While we recently demonstrated that TIMP2
82 is critical in revitalizing overall hippocampus-dependent cognitive function in aged mice
83 (Castellano et al., 2017), the biological role of TIMP2 expressed within the hippocampus, where
84 it is highly expressed, has not been studied. TIMP2 is part of a small family of tissue
85 metalloproteinase inhibitors that include TIMP1, TIMP3, and TIMP4, all of which perform broad
86 MMP targeting functions but in diverse contexts in the brain, including in myelin repair (Nicaise et
87 al., 2019), neurovascular regulation (Dewing et al., 2019), or in regulation of the tumor
88 microenvironment (Solga et al., 2019). Interestingly, TIMP2 shares only ~40-50% sequence
89 homology with other TIMP family members and is particularly expressed in the brain and enriched
90 specifically in hippocampus relative to other TIMPs. Since levels of TIMP2 decline in the
91 hippocampus with age (Castellano et al., 2017), understanding the function of this local source
92 will be important to understand its normal function and position it for putative therapies age-related
93 brain disorders. Moreover, we sought to understand the extent to which ECM regulation is related
94 to disparate processes of plasticity to regulate complex behavioral outputs.

95 Here we define a mechanism by which TIMP2 regulates ECM components in the
96 hippocampus in a manner that regulates processes linked to plasticity and memory. We find that
97 TIMP2 is predominantly expressed by neurons in the hippocampus and is present at high levels
98 in the brain extracellular space adjacent to these cells. Deletion of TIMP2 induces transcriptomic
99 changes in the hippocampus that are consistent with processes related to synaptic plasticity and
100 adult neurogenesis. We find that loss of TIMP2 results in fewer dendritic spines in dentate gyrus
101 (DG) granule cells, decreased adult DG neurogenesis along several stages, and impaired
102 memory in various hippocampus-dependent tasks. Loss of TIMP2 also causes an accumulation
103 of ECM proteins, particularly around synapses within the DG, and impaired migration of

104 neuroblasts within the neurogenic niche, reflecting dysregulated ECM turnover. Finally, we
105 developed a mouse model for conditional deletion of TIMP2 from neurons that exhibits the
106 functional phenotypes observed in TIMP2 KO mice, further arguing for a role of the neuronal pool
107 of TIMP2 in shaping plasticity-related function of the hippocampus. Our findings indicate
108 molecular mechanisms through which neuronal TIMP2 remodeling of the ECM promotes synapse
109 plasticity and is required for memory, with functional implications for neurogenic rejuvenation.
110

111 **Materials and Methods**

112 **Animals**

113 All animal care and procedures were performed in accordance with the National Institutes of
114 Health Guide for Care and Use of Laboratory Animals and the Icahn School of Medicine at Mount
115 Sinai Institutional Animal Care and Use Committee. All efforts were made to reduce the number
116 of animals used and to minimize their suffering and pain. TIMP2 knockout (KO) (Jackson) and
117 WT female mice or $Syn^{Cre/+}$; $TIMP2^{fl/fl}$ and $TIMP2^{fl/fl}$ mice were used at 2-3 months or 5-6 months
118 of age unless indicated otherwise. Littermate controls were used for all experiments. Mice were
119 maintained on a 12h light/dark cycle at constant temperature (23°C) with *ad libitum* access to food
120 and water.
121

122 **Generation of TIMP2-floxed mice**

123 To achieve conditional deletion of *Timp2*, a loxP-flanked *Timp2* allele ($TIMP2^{fl/fl}$) was generated
124 by the two-cell homologous recombination (2C-HR)-CRISPR/Cas9-based genome editing
125 method, as previously described (Gu et al., 2018). Briefly, two loxP sites were inserted into the
126 *Timp2* gene flanking exon 2, with homologous arms (HA) on each side. Two point-mutations
127 (C928->A near the end of the left arm and G1795->T at the 5' junction of the right arm) were
128 introduced to disrupt the PAM sequence to avoid re-cutting of the recombined allele. Three
129 nucleotides adjacent to each loxP site were altered to create restriction sites for diagnostic

130 purposes: XbaI near the upstream loxP, and HindIII near the downstream loxP site. The two-cell
131 stage embryo microinjection procedure was performed as in (Gu et al. 2018), using Cas9-mSA
132 mRNA, biotinylated double-stranded PCR product (1016 nts), and pre-assembled ctRNA
133 prepared accordingly (Gu et al., 2018). F_0 mice were screened by sequencing from TOPO cloned
134 PCR product, using tail genomic DNA, amplified from the TIMP2 target region, and using the
135 following primers: FW-AGCGACCGATAAGCAGGAAG, Rev-CACTAGCAGACACCACCACA.
136 Identified founders were crossed with wild-type (WT) C57BL/6J mice, purchased from The
137 Jackson Laboratory, to produce heterozygous mice.

138 To achieve neuron-specific *Timp2* deletion, neuron-specific heterozygous Synapsin (Syn)-
139 Cre ($Syn^{Cre/+}$) transgenic mice (Zhu et al., 2001) (JAX stock #003966) were crossbred with
140 $TIMP2^{fl/fl}$ mice to generate $Syn^{Cre/+}$; $TIMP2^{fl/+}$ progeny. The F_1 mice were then crossed to generate
141 $Syn^{Cre/+}$; $TIMP2^{fl/fl}$ and $TIMP2^{fl/fl}$ littermate controls. Cre expression was maintained in the female
142 mice for breeding (Zhu et al., 2001). All animals were maintained on a C57Bl/6J background.
143

144 **Genotyping**

145 Genotyping of $TIMP2^{fl/fl}$ mice was performed using the following primers: *Primer 1*: 5'-
146 TGACCCCTCTGCTCTAGTCC, *Primer 2:* 5'-GCTCCGTCTCTTCGTCCATC (**Figure 6A**).
147 Genomic DNA was extracted from the tail using the QIAamp Fast DNA Tissue Kit (Qiagen). PCR
148 was performed in a total volume of 50 µl at 94°C for 2 min, 94°C for 30 s, 61°C for 30 s, 68°C for
149 2 min and 15 sec for 10 cycles, then 94°C for 30 s, 56°C for 30 s, 68°C for 2 min and 15 s for 25
150 cycles, and ending at 72°C for 5 min using Prime STAR (#R050A, TaKaRa). For loxP site
151 verification based on restriction digest, the PCR product (2.1 kb) was digested with XbaI and
152 HindIII restriction enzymes (New England Biolabs, Ipswich, MA) at 37°C for 1 hour, followed by
153 10 min at 65°C for heat inactivation. Digested PCR products were run on an agarose gel and
154 imaged for the identification of founders: HindIII (Wt: 2133 bp; upstream loxP positive: 829 bp and
155 1,304 bp); Xba1 (Wt: 2133 bp; downstream loxP positive: 566 bp and 1,567 bp).

156

157 **In vivo microdialysis**

158 For guide cannula implantation into the hippocampus, mice were anesthetized with 2% isoflurane
159 and hair over the skull was shaved prior to being fixed in a stereotaxic apparatus (Stoelting Co.,
160 Wood Dale, IL, USA). After preparing skin with 70% ethanol and povidone-iodine, an anterior-to-
161 posterior incision was made along the midline of the head to expose the skull. Skull position was
162 leveled to within 0.1 mm along the bregma-lambda axis, and at 2.2 mm to the left and right of
163 midline on the lateral axis. Holes were drilled to target the left hippocampus using the stereotaxic
164 coordinates: bregma -3.1 mm, 2.5 mm lateral. A second hole was made diagonally to the first, to
165 serve as an anchoring position with a bone screw. To target caudal hippocampus, AtomosLM
166 Guide Cannula (PEG-12, Eicom, San Diego, CA, USA) was inserted at a 12° angle, 1.2 mm below
167 the dura mater. Dental cement was applied to secure the cannula, and the skin was secured using
168 a surgical adhesive glue. An AtmosLM Dummy Cannula (PED-12, Eicom, San Diego, CA, USA)
169 was inserted into the guide cannula and secured with a plastic cap nut. Animals were then placed
170 in a clean cage on a heating pad and allowed to recover from surgery.

171 Approximately 12 hours following surgery, mice underwent 1000-kDa *in vivo* microdialysis.
172 The inlet port of AtmosLM Microdialysis Probe (PEP-12-02, Emicon) was connected to a syringe
173 pump (kdScientific) perfusing artificial CSF (aCSF; in mM: 1.3 $CaCl_2$, 1.2 $MgSO_4$, 3 KCl, 0.4
174 KH_2PO_4, 25 $NaHCO_3$, 122 NaCl, pH 7.35) at a rate of 1.2 µl/min (Ulrich et al., 2013). The outlet
175 of the probe was connected to the peristaltic pump (MAB 20, SciPro), which was calibrated to
176 obtain a pull rate between 1-1.1 µl/min. After the probe was connected to the push-pull
177 mechanism, the mice were briefly anesthetized with isoflurane to allow for the removal of the
178 dummy cannula and insertion of the probe into the hippocampus. The probe was secured with a
179 cap nut, and a plastic collar was loosely placed around the mouse neck. Mice were then moved
180 to a Raturn (Stand-Alone Raturn System, BASi, West Lafayette, IN, USA) and tethered by the
181 collar to avoid tangling microdialysis tubing (FEP tubing 0.65 mm OD x 0.12 mm ID, BASi), while

182 allowing for free movement of the mouse during the sample collection period. Samples were
183 collected hourly in a refrigerated fraction collector (MAB 85 Fraction Collector, SciPro) and frozen
184 after collection at −80°C. The procedure was performed under constant light conditions, and food
185 and water were provided *ad libitum*.
186
187 **Bulk RNA-sequencing**
188 RNA-sequencing was performed on hippocampi dissected from WT and TIMP2 KO male and
189 female mice. Dissected hippocampi were preserved in RNAlater (Invitrogen, Carlsbad, CA)
190 overnight at 4°C before storing at −80°C until use. RNA was extracted using the RNeasy Mini Kit
191 (Qiagen), according to the manufacturer's instructions. RNA quality was measured using the
192 Agilent TapeStation Bioanalyzer (Agilent Technologies, USA), and all samples exhibited RNA
193 Integrity Number (RIN) > 8. cDNA libraries were prepared with poly(A) selection and sequenced
194 using Illumina Hiseq (2x150bp paired-end) (Genewiz). At least 25 M clean reads were generated
195 from each sample. The reads were mapped to the *Mus musculus* GRCm38 reference genome
196 available on ENSEMBL, using STAR aligner (v.2.5.2b). After extraction of gene hit counts, the
197 gene hit counts table was used for downstream differential expression analysis, using DESeq2
198 software. The Wald test was used to generate *P*-values and log2 fold changes. Differentially
199 expressed genes (DEGs; $P<0.05$) were used for Gene Set Enrichment Analysis (GSEA;
200 https://www.gsea-msigdb.org/gsea/index.jsp). Volcano plot was generated with R v4.1.2.
201
202 **BrdU injections**
203 For cell proliferation assessment, mice were injected intraperitoneally (i.p.) once with 5-Bromo-2′-
204 deoxyuridine (BrdU; Sigma) at a concentration of 150 mg/kg dissolved in 0.9% sodium chloride
205 solution and sacrificed 24 hours later. For cell fate ("survival") analysis, an additional group of
206 mice was i.p.-injected with BrdU once a day for 5 consecutive days, followed by a chase period
207 of 28 days before perfusion.

208

209 **Immunohistochemistry and microscopy**

210 For all immunohistochemistry experiments, mice were anesthetized with a cocktail of ketamine
211 (90 mg/kg) and xylazine (10 mg/kg) and transcardially perfused with ice-cold 0.9% saline. Brains
212 were dissected, and hemibrains isolated for immunohistochemistry were postfixed in 4%
213 paraformaldehyde (PFA) for 48 hours at 4°C before preservation in 30% sucrose (Sigma) solution
214 in phosphate-buffered saline (PBS). Hemibrains were sectioned coronally at 40-μm thickness on
215 a freezing-sliding microtome (SM2010R, Leica), and sections were stored in cryoprotective
216 medium at −20°C.

217 For immunohistochemistry, free-floating brain sections were permeabilized with Tris-
218 Buffer Saline (TBS) plus 0.05% Tween (TBST) and incubated in a blocking solution consisting of
219 10% normal goat (#S-1000, Vector Laboratories) or donkey serum (#017-000-121, Jackson
220 ImmunoResearch) in TBST. Sections were then incubated with primary antibodies in 2% goat or
221 donkey serum in TBST overnight at 4°C. Sections were incubated with primary antibodies,
222 including the following: TIMP2 (1:100; #AF971, R&D Systems), NeuN (1:200; #MAB377,
223 Millipore), doublecortin (DCX; 1:200; #4604S, Cell Signaling), Sox2 (1:200; #sc365823, Santa
224 Cruz), Ki67 (1:200; #14-5698-82, Invitrogen), aggrecan (1:500; #AB1031, Millipore), Homer1
225 (1:500; #160006, Synaptic Systems). The next day, sections were washed in TBST three times
226 for 5 min each and incubated with Alexa Fluor-conjugated secondary antibodies at 1:200 in TBST
227 for 1 hour at RT. Secondary antibodies used were: Alexa Fluor 594-labeled donkey anti-rabbit
228 (#A21206), Alexa Fluor 594-labeled donkey anti-mouse (#A21203), Alexa Fluor 488-donkey anti-
229 rat (#A21208), Alexa Fluor 488-donkey anti-goat (#A11055), Alexa Fluor 647-donkey anti-mouse
230 (#A31571), Alexa Fluor 594-goat anti-rabbit (#A11012), Alexa Fluor 5488-goat anti-chicken
231 (#A11039), all from Life Technologies. Brain sections were then washed, stained with 4′,6-
232 diamidino-2-phenylindole (DAPI, Sigma-Aldrich) for 15 min to visualize nuclei, mounted and
233 coverslipped using Prolong Gold (Life Technologies) and dried overnight before imaging. For

234 BrdU staining, brain sections were pre-treated with 3M HCl (Thermo Fisher) for 30 min at 37°C
235 before overnight incubation with primary antibody anti-BrdU (1:500; #ab6326, Abcam) at 4°C.
236 Secondary staining and mounting were performed as described above.
237 Image processing was performed using an LSM 780 confocal microscope (Zeiss,
238 Oberkochen, DE) using 40x/1.4 Oil DIC objective. Four equally-spaced sections per mouse
239 (rostral through the caudal extent of the DG) were used to count the total number of positive cells
240 within the DG (subgranular zone and hilar subregions) of the hippocampus according to
241 stereological principles. All counts were performed using FIJI in a blinded fashion.
242
243 **Aggrecan and Homer1 puncta quantification**
244 Quantification of the number of puncta by super-resolution microscopy proceeded similar to the
245 method described in (Nguyen et al., 2020). Briefly, images were acquired by confocal microscopy
246 imaging using an LSM 880 with AiryScan in super-resolution mode (Zeiss) set with a 63X/1.4 Oil
247 DIC objective with 5X optical zoom. Using consistent laser strength, gain, and digitial offset
248 settings across all sections/experiments, Z stacks were acquired with steps less than the optical
249 slices acquired. Using Zen software (Zeiss), a setting of 6 ("optimal") was used during AiryScan
250 processing. Aggrecan puncta were quantified using the Puncta Analyzer plugin (Ippolito and
251 Eroglu, 2010) in ImageJ, and thresholding was applied equally across images. For colocalization
252 of co-stained Aggrecan and Homer1 puncta, images were analyzed with the Puncta Analyzer
253 plugin with a minimum pixel specification of 4. Three images in the molecular layer of the DG
254 were averaged per mouse for analysis.
255
256 **Dendritic spine analysis by iontophoretic dye injections**
257 *Tissue processing.* Mice were anesthetized using 30% chloral hydrate and transcardially perfused
258 with 1% PFA in phosphate buffer (PB, pH 7.4) for 2 min, followed by 4% PFA with 0.125%
259 glutaraldehyde in PB for 10 min at a rate of 5 ml/min. Brains were dissected and postfixed

260 overnight at 4°C in the same fixative, and then transferred to PBS with 0.1% sodium azide at 4°C
261 until sectioned. Brains were hemisected, and the right hemisphere was cut into 250 μm-thick
262 sections using a vibratome (VT1000S, Leica Microsystems, Buffalo Grove, IL).
263 *Intracellular dye injection and confocal imaging*. Coronal sections were incubated in 250 ng/ml
264 DAPI for 5 min to enable identification of the DG. Sections were mounted on nitrocellulose
265 membrane filters, immersed in ice-cold PB, and DG granule cells were iontophoretically injected
266 with 5% Lucifer Yellow (Invitrogen, Carlsbad, CA) in distilled water under a direct current of 3-8
267 nA until the dye filled the distal ends of the dendrites. Six to eleven neurons were injected per
268 section and neurons selected for injection were spaced to avoid overlapping of dendrites.
269 Sections were mounted with Fluoromount-G (#0100-01, Southern Biotech, Birmingham, AL) on
270 gelatin-coated glass slides (#22-214-320, Fisher).
271 To select dendritic segments for imaging on a Zeiss LSM 780 confocal microscope (Zeiss),
272 whole cells were first imaged at 20x/0.8 M27 Plan-Apochromat objective, using an Ar/Kr laser at
273 an excitation wavelength of 488 nm. Confocal stacks were acquired at 512 x 512-pixel resolution
274 with a Z-step of 1 μm, a pinhole setting of 1 Airy Unit, and optimal settings for gain and offset.
275 Basal dendritic segments at 50 μm from the soma were selected for high-resolution imaging
276 according to the following criteria: not a primary dendrite, no overlap with other dendrites or
277 branching that would obscure spines, not too deep in the section, and parallel or at acute angles
278 to the coronal plane. Dendritic segments were imaged using a 100x/1.46 Oil DIC M27 Plan-
279 Apochromat objective, and stacks were acquired at 512 x 512-pixel resolution with a Z-step of 0.1
280 μm, optical zoom of 3.3x, a pinhole setting of 1 Airy Unit, and optimal settings for gain and offset.
281 The stacks were imaged with approximately 1 μm above and below the segment to fully include
282 all spines. Three z-stacks were imaged from each neuron. Confocal stacks were deconvolved
283 using an iterative blind deconvolution algorithm (AutoQuant X, vX3.0.1, MediaCybernetics,
284 Bethesda, MD).
285

286 *Spine reconstruction and analysis.* Deconvolved stacks were analyzed using Neurolucida 360
287 (v2019.2.1; MBF Bioscience) for semi-automated reconstruction of dendrites and spines to
288 determine spine density and morphology. Spines were classified as stubby, thin, mushroom, and
289 filopodia morphologies. 4-5 mice per genotype, 6 neurons per mice, and 3 dendrites per neuron
290 were analyzed, and violin plots were used to better visualize the distribution of individual data
291 points.
292
293 **Scanning electron microscopy (SEM)**
294 Following ketamine/xylazine anesthesia and transcardial perfusion with PBS, 2-mm thick brain
295 slices containing the hippocampus were decellularized, following previously described methods
296 (De Waele et al., 2015). SEM methods were adapted from a previous study (Tajerian et al., 2018).
297 Decellularized brain slices were fixed in 4% PFA with 2% glutaraldehyde in 0.1M sodium
298 cacodylate buffer (pH 7.4) for 24 hours at 4°C. Samples were then briefly rinsed in the same
299 buffer before post-staining with 1% OsO4 for 1 hour. OsO_4-treated samples were rinsed in water
300 and gradually dehydrated in increasing concentrations of ethanol (50, 70, 90 100, 100%, 10 min
301 each). Samples were then stacked horizontally onto wire mesh dividers to keep them flattened
302 and critical point-dried with liquid CO_2. Dried samples were mounted onto Aluminum SEM stubs
303 using conductive copper tape and sputter-coated before imaging with a Zeiss Supra 55 VP
304 FESEM using InLens SE detection at 5 kV operating voltage (Carl Zeiss Microscopy Inc, USA).
305 Fiber diameters were analyzed using Image J (Bethesda, USA).
306
307 **Behavior**
308 All behavioral analyses were performed during the 0700–1900 light cycle. For all behavioral
309 experiments, age- (2-3 months old) and sex-matched mice with corresponding littermate control
310 animals were used.

311

312 *Novel location recognition.* Hippocampus-dependent memory was assessed using the novel
313 location recognition as previously described (Castellano et al., 2017). On day 1, the training day,
314 mice were habituated to the open-field arena for 6 min, an arena that contained wall-mounted
315 visual cues. Mice were exposed to three consecutive trials of 6 min each, during which they
316 explored two different objects in fixed positions. On day 2, the testing day, mice explored the
317 same arena as on the training day but with one object displaced to a novel position. Time spent
318 exploring each object was manually scored in a blinded fashion to assess the discrimination index
319 for the novel location as the displaced object interaction time/total interaction time of both objects.
320

321 *Contextual fear-conditioning.* Fear-conditioning experiments were performed as previously
322 described (Castellano et al., 2017) to assess hippocampus-dependent memory. Briefly, mice
323 were trained to associate the cage context with an aversive stimulus (light foot-shock; Ugo Basile).
324 On the first day, training parameters included two periods of 30 s consisting of a paired cue light
325 and a tone of 1,000-Hz, followed by a light foot-shock (2 s, 0.5 mA) separated by a 180-s interval.
326 Chambers were cleaned with 70% ethanol between experiments by the experimenter. Twenty-
327 four hours later, mice were re-exposed to the same context for 3 min, and freezing levels
328 (contextual) were measured. Two hours later, for the cued task, mice were placed in a novel
329 context and exposed to the same tone and cue light from day 1 (training) after 120 s of exploration.
330 Freezing levels were analyzed for pre- and post-cue phases. Freezing levels were measured
331 using EthoVision XT system software (v14.0.1319, Noldus).
332

333 *Barnes maze.* Barnes maze testing was performed similarly to that previously described
334 (Castellano et al., 2017). A large circular maze containing 40 holes was centered over a pedestal
335 and elevated approximately 40 cm above the floor with a video recording device mounted directly
336 above. The escape hole consisted of a PVC box similar in texture and color to the surface of the

maze. Distinct visual cues were placed at four equally spaced points around the maze to serve as spatial navigation cues as the mice navigate the task. The task proceeded over 4 days, with four trials on each day for each mouse. With overhead illumination and a persistent 2 kHz tone, mice were given 90 s for each trial to identify the escape hole by jumping in or identifying the hole with extended/overhead pokes. If mice failed to find the escape hole within 90 s, mice were gently guided by light tapping/directing towards the escape hole and scored with 90 s. The escape hole position was fixed within a day but changed for each successive day of testing. For each trial within a day, the starting location for the mouse was rotated relative to the escape hole position. Data collection and analyses were performed using EthoVision video-tracking system.

Search strategy classification was manually performed and based on methods adapted from previous work (Mateus-Pinheiro et al., 2017), with data collected by EthoVision video-tracking system software. Search strategies were coded according to the following: (i) localized - minimal movement from the starting position; (ii) serial - sequential nose points within the outer ring area; (iii) random - unorganized searching; (iv) scanning - arc-like trajectory, without nose points; (v) focal - direct search within a maze quadrant; (vi) focal missense - direct search within a maze quadrant from previous trials; (vii) targeted - direct movement to hole with deviations in the trajectory direction; (viii) direct - no shifts in the trajectory direction with single nose point to target hole. For strategy analysis, each related strategy was categorized into non-hippocampus-dependent strategies comprising localized, serial, random, and scanning strategies, and hippocampus-dependent strategies that included focal, focal missense, targeted and direct strategies. Cognitive performance of each trial on day 3 was scored such that cognitive strategies received higher scores according to the following scale, accounting for high cognitive complexity, with a separation of 1 point between non-hippocampus-dependent and hippocampus-dependent strategies: localized = 0, serial = 1, random = 2, scanning = 3, focal = 5, focal missense = 5, targeted = 6, direct = 6. Focal and focal missense strategies are assigned a score of 5 since both are goal-directed strategies used without achieving the final target. Target and direct strategies

363 were assigned score of 6 since both are goal-directed strategies with successful achievement of
364 the final target.
365
366 *Open field*. The open field test was used to evaluate locomotion and exploratory behavior, and
367 anxiety-like behavior in the center of the arena. The apparatus consisted of a brightly illuminated
368 square arena of 50 x 50 cm closed by walls 45 cm high. Mice were placed individually in the
369 center of the open field arena, and their movement was traced for 6 min. The resulting data was
370 analyzed using EthoVision software, considering two previously defined areas: a central and an
371 outer area. Due to the thigmotaxic exploratory activity of rodents, the ratio between the time spent
372 in the center and in the periphery of the open field arena can reflect anxiety-like behaviors.
373 Distance traveled, average velocity, and time spent in each of the zones were recorded and
374 analyzed.
375
376 *Rotarod*. Balance and motor function was measured using the fixed and standard accelerated
377 rotarod test (Med Associates, St. Albans, VT). The protocol consisted of a first day of training at
378 a constant speed (4 rpm) for a maximum of 2 min in three trials, with a 2-min interval between
379 each trial. On day 2, animals were tested for each of 3 different fixed speeds over a range of 4 to
380 40 rpm for a maximum of 60 sec each in three trials, with a 2-min interval between each trial. For
381 the acceleration test, animals were placed on the rod rotating at a constant speed (4 rpm), then
382 the rod started to accelerate continuously from 4 to 40 rpm over 5 min, in three trials with a 5-min
383 interval between each trial. The latency to fall off the rotarod was recorded for each trial, and data
384 from three trials were averaged for each mouse.
385
386 *Wire grip test.* Motor coordination and strength was measured by the wire grip task. Each mouse
387 was placed on a wire cage top, which was slowly inverted and suspended at approximately 30
388 cm above a mouse cage. The latency of time until the mouse fell off the wire was recorded in

389 three trials. Mice that did not fall within the 60-s trial period, were removed and assigned a
390 maximal time of 60 s. Data from three trials were averaged for each mouse.
391
392 *Clasping.* Mice were suspended by their tail, and the extent of hindlimb clasping was observed
393 for 15 s. Clasping scoring was based on a previously described method (Zhu et al., 2016). Briefly,
394 if both hindlimbs were splayed outward away from the abdomen with splayed toes, a score of 0
395 was given. If one hindlimb was retracted or both hindlimbs were partially retracted toward the
396 abdomen without touching it, and the toes were splayed, a score of 1 was assigned. If both
397 hindlimbs were partially retracted toward the abdomen and were touching the abdomen without
398 touching each other, a score of 2 was given. If both hindlimbs were fully clasped and touching the
399 abdomen, a score of 3 was assigned.
400
401 *Grip strength.* For the grip strength test, forelimb, hindlimb, and 4-limbs grip strength was
402 evaluated using a grip strength meter (Bioseb). Animals were held by the tail and allowed to place
403 forelimbs on the bar, or they were restrained to place hindlimbs on the bar connected to the force
404 sensor. Mice were slowly pulled away until they released the bar, and the maximal grip force
405 measured during the pulling session was recorded. For the 4-limb measurement, using a mesh
406 pull bar attachment, animals were handled by the tail so that all the paws latching onto the mesh
407 pull the bar together. The mice were slowly and steadily pulled away from the apparatus exactly
408 parallel from the countertop until paws were released from the mesh. A modified version of the
409 forelimb grip strength test was performed as previously described (Takeshita et al., 2017). Briefly,
410 the meter was rotated vertically and the measurement procedure was identical to the conventional
411 test, except for the direction in which the mouse's tail was pulled. Each animal's grip strength (in
412 *g*) was recorded, and data from five trials were collected.
413

414 *Pole test.* Motor coordination and balance with striatal involvement was assessed with the vertical
415 pole test, which consisted of a plastic pole (50 cm high, diameter 1 cm) placed vertically on a
416 mouse cage. Mice were individually placed at the top of the pole facing upward by their front paws
417 on the pole, and the time taken to turn around and climb down the pole was recorded. A maximum
418 time of 120 s was given to complete the task. If the mouse fell from the top of the pole, a time of
419 120 s was recorded. Each mouse underwent three trials, and the pole was cleaned with 70%
420 ethanol between animals. Data from three trials were averaged for each mouse.
421
422 **qPCR**
423 After rapid dissection of the hippocampus, tissue was preserved in RNAlater (Invitrogen)
424 overnight at 4°C before storing at −80°C until use. Hippocampal RNA was extracted according to
425 the manufacturer's instructions using a RNeasy Mini Kit (Qiagen). Quality and concentration of
426 total RNA were measured on the Nanodrop 8000 (Thermo Scientific). cDNA was subsequently
427 synthesized with SuperScript III (Invitrogen), following the manufacturer's recommendations.
428 Samples were mixed with SYBR Green master mix (Thermo Fisher) and primers for Mmp2 (FW:
429 5'-CAAGTTCCCCGGCGATGTC-3'; REV: 5'-TTCTGGTCAAGGTCACCTGTC-3') before loading
430 as technical replicates for qPCR on a QuantStudio 7 Flex Real-Time PCR System (Thermo
431 Scientific). Cycle counts for mRNA quantification were normalized to *Rplp0* (FW: 5'-
432 AGATTCGGGATATGCTGTTGGC-3'; REV: 5'-CCAGTTGGTAACAATGCCATGT-3'). The ΔΔCT
433 method was used to provide gene expression values, and expression levels were normalized to
434 *Rplp0*.
435
436 **Western blotting**
437 For Western blotting of MMP2 or TIMP2 within hippocampus, dissected hippocampi were
438 manually homogenized with 60 strokes in RIPA lysis buffer (Thermo Fisher), with protease
439 inhibitors (Roche), before centrifugation at 20,000g for 25 min at 4°C. Protein concentration of the

440 supernatant was determined using the BCA kit (Thermo Fisher). Samples with equal amounts of
441 protein were separated on 4-12% NuPAGE Bis-Tris precast denaturing gels (Invitrogen) and
442 transferred onto nitrocellulose membranes (BioRad) at 125 V for 90 min. Membranes were
443 blocked with 3% milk-TBST (0.125% Tween) for 1 hour at RT and then probed with primary
444 antibodies diluted in 3% milk-TBST solution overnight at 4°C: anti-TIMP2 (1:500; #D18B7, Cell
445 Signaling), anti-MMP2 (1:1000; #ab86607, Abcam), and anti-actin (1:10000; #A5060, Sigma).
446 Membranes were washed and probed with horseradish-peroxidase-conjugated anti-mouse
447 (1:15,000; #1705047, BioRad) or anti-rabbit (1:15,000; #1705046, BioRad) for 1 hour at RT.
448 Membranes were developed using ECL Clarity reagent (BioRad) and imaged using ChemiDoc
449 MP Imaging System and Image Lab software (BioRad). Band intensities were quantified using
450 ImageJ software as previously described (Castellano et al., 2011).
451 For TIMP2 detection in ISF samples, 4 consecutive baseline eISF samples from
452 microdialysis were pooled and concentrated ~6 fold using Pierce Concentrator (PES, 3K MWCO,
453 Thermo Scientific). Concentrated samples were then processed for western blotting as described
454 above. Estimation of eISF TIMP2 protein levels was determined by extrapolation from a standard
455 curve of recombinant mouse TIMP2 (R&D/Biotechne) ranging from 0.31 ng to 20 ng run alongside
456 ISF samples in SDS-PAGE/Western that had been concentrated ~9.2-fold.
457
458 **Data analysis**
459 Statistical analyses were performed using GraphPad Prism version 9.0 software (GraphPad
460 Software, San Diego, California USA). Statistical tests are as described in text and figure legends,
461 including the use of student's *t* test for 2-group comparisons, nested *t* tests with multi-level
462 variables for 2-group comparisons, or chi-square analysis for 2-group comparisons of proportions.
463 All experiments were performed in a randomized and blinded fashion.
464
465 **Results**

466 **TIMP2 is expressed in hippocampal neurons, and its deletion induces transcriptomic**
467 **changes**

468 TIMP2 exhibits high expression in the hippocampus relative to other brain regions
469 (Castellano et al., 2017). To identify the cellular sources of TIMP2 in the hippocampus and to
470 begin to probe its function in this region, we examined TIMP2 protein levels by confocal
471 microscopy in various subfields of the hippocampus of 2-month-old wildtype (WT) male and
472 female mice. We found that TIMP2 is expressed in the hilus of dentate gyrus (DG), as well as
473 CA3 and CA1 subfields of the hippocampus, and we found that the majority of TIMP2-expressing
474 cells co-localized with staining for pan-neuronal marker, NeuN, arguing that the major cellular
475 source of TIMP2 expression in these areas was neuronal (**Figure 1A, 1B**). We did not detect
476 differential TIMP2 neuronal expression in the hilus/DG, CA3, and CA1 subfields between males
477 and females (**Figures S1A-C**).

478 Given the high level of TIMP2 expression seen in neurons in the hippocampus, we asked
479 whether levels were elevated in the extracellular space adjacent to this cellular source. To
480 measure extracellular levels of TIMP2 in this region, we implanted high molecular-weight cut-off
481 (1-MDa) probes into hippocampi of freely moving, 2-3-month-old WT mice to measure interstitial
482 fluid (ISF) levels of TIMP2 by *in vivo* microdialysis. TIMP2 was readily detectable in the ISF in
483 hippocampus (**Figure 1D**), and extrapolated values of exchangeable ISF TIMP2 were ~10.1 ±
484 0.16 ng/mL (N=3), as measured at a flow rate of 1 µl/min. Importantly, the 21- to 22-kDa TIMP2
485 band was absent in the ISF of hippocampus from mice in which TIMP2 has been deleted (KO)
486 (**Figure 1D**).

487 The high levels of TIMP2 within neurons and the extracellular space of the hippocampus
488 argues for unappreciated roles for its function locally in this region, prompting us to examine the
489 cellular and molecular processes regulated by TIMP2. In order to identify putative pathways
490 involved in TIMP2 function in the hippocampus, we isolated hippocampi from WT and TIMP2 KO
491 male and female mice and processed the tissue for RNA-sequencing (**Figure 1E**). A total of 905

492 differentially expressed genes (DEGs; *P<0.05*) were identified in TIMP2 KO compared to WT
493 (**Figure 1F**), with TIMP2 being the top differentially expressed gene, as expected. Of these genes,
494 449 DEGs were downregulated in TIMP2 KO hippocampi (**Figure 1F**). To gain insights into how
495 the altered transcriptome may reflect altered biological processes, we performed gene set
496 enrichment analysis (GSEA). Downregulated DEGs in TIMP2 KO were enriched for a number of
497 Gene Ontology (GO) biological processes related to plasticity, including "cell morphogenesis",
498 "neurogenesis", "cell projection organization", and "synapse organization" (**Figure 1G**).
499 Upregulated DEGs in TIMP2 KO were enriched in functions that included "regulation of cell death
500 and cell cycle", among others (**Figure S1E**). Together, our data suggest that TIMP2 in the normal
501 hippocampus may be involved in processes of plasticity.
502
503 **TIMP2 is necessary for adult neurogenesis in the normal dentate gyrus**
504 To evaluate the extent to which our discovery-based pathway approach from RNAseq highlighted
505 processes that may indeed be regulated by TIMP2, we examined the key cellular processes
506 implicated. As one of the top downregulated pathways in hippocampus of TIMP2 KO vs. WT mice
507 was "neurogenesis", we used confocal microscopy to begin to address whether processes of adult
508 neurogenesis within the DG are altered by absence of TIMP2. To examine whether TIMP2
509 regulates overall cell proliferation, we injected WT and TIMP2 KO mice with the proliferation
510 marker bromodeoxyuridine (BrdU), which labels the pool of proliferating cells in the subgranular
511 zone (SGZ) of DG (**Figure 2A**). We found that the DG of TIMP2 KO mice had significantly fewer
512 proliferating cells than in WT mice (**Figure 2C)**, as quantified by the total number of $BrdU^+$ cells
513 (**Figure 2D**). We observed a similar result when analyzing the pool of $Ki67^+$ cells in the SGZ
514 (**Figure 2E-F**), which marks a larger pool of proliferating cells in other phases. We next analyzed
515 the pool of neural progenitor cells and the immature neuroblasts they ultimately give rise to, using
516 SRY-Box Transcriptional Factor 2 (Sox2) and doublecortin (DCX) markers, respectively. Deletion

517 of TIMP2 resulted in a significant decrease in the number of Sox2$^+$ neural progenitor cells (**Figure**
518 **2G-H**), and of DCX$^+$ immature neurons (**Figure 2I-J**).
519 To examine whether this disrupted pool of neuroblasts corresponds to a differing number
520 of surviving immature neurons, we injected TIMP2 KO and WT mice by pulse-chase labeling with
521 BrdU for 5 days and quantified the number of label-retaining, surviving BrdU$^+$ NeuN$^+$ neurons in
522 the SGZ of DG 4 weeks later (**Figure 2B**). Using this paradigm, we found that the DG of TIMP2
523 KO mice had significantly fewer newborn neurons compared with the DG of WT mice (**Figure 2K-**
524 **L**). Together, these results are consistent with TIMP2-mediated roles in adult neurogenesis and
525 related pathways uncovered by our transcriptomic analysis.
526
527 **TIMP2 regulates dendritic spine plasticity in the dentate gyrus**
528 Our transcriptomic data in TIMP2 KO hippocampi suggest a role for TIMP2 acting within the
529 hippocampus to modulate plasticity processes, including "synapse organization", possibly at the
530 structural level. To evaluate the impact of TIMP2 deletion on dendritic spines, the cellular
531 substrates of memory storage (Yang et al., 2009), we turned to a rigorous method to sensitively
532 quantify dendritic spines and their classification. We performed Lucifer Yellow iontophoretic dye-
533 filling of mature DG granule cells in isolated slices from TIMP2 KO and WT mice for high-
534 resolution imaging and reconstruction (**Figure 3A**) (Dickstein et al., 2016; Price et al., 2014). We
535 found that neurons in the DG of TIMP2 KO mice exhibited significantly reduced dendritic spine
536 density compared to those in WT DG (**Figure 3B, E**). We then used automated classification
537 algorithms (Dickstein et al., 2016; Rodriguez et al., 2008) to classify and quantify spines based
538 on morphology, as a readout of spine plasticity. Intriguingly, we found a significantly higher
539 proportion of immature thin spines in labeled DG neurons from TIMP2 KO mice compared to
540 those in WT mice (**Figure 3C, E**) and a significantly decreased proportion of mature mushroom
541 spines (**Figure 3D, E**) exhibited by TIMP2 KO relative WT DG neurons. Mushroom spines are a
542 particularly stable class of spines with lower turnover (Bourne and Harris, 2007) and are proposed

543 to serve as structural correlates of memory (Zuo et al., 2005). Of note, these described spine
544 observations in DG neurons of TIMP2 KO mice are in line with previous descriptions of altered
545 synaptic function upon TIMP2 modulation (Castellano et al., 2017), including long-term
546 potentiation, which was shown to be affected by modulating levels of TIMP2 (Castellano et al.,
547 2017). Collectively, these results suggest that TIMP2 may act to promote plasticity through
548 regulation of adult neurogenesis and dendritic spine formation.
549

550 **TIMP2 is required for hippocampus-dependent memory function**

551 The hippocampus is critical for spatial memory and learning, likely through regulation of adult
552 neurogenesis in the DG [reviewed in (Anacker and Hen, 2017)], as well as through changes in
553 synaptic structure (Jedlicka et al., 2008; Moser et al., 1994). The changes we observed in both
554 adult neurogenesis and dendritic spine plasticity in TIMP2 KO hippocampi prompted us to
555 investigate whether TIMP2 is involved in hippocampus-dependent memory and learning. We first
556 utilized the novel location recognition task (**Figure 4A**), in which mice use spatial cues in the
557 arenas to learn and associate the positions of objects in space. 24 hours after training, we
558 observed that TIMP2 KO mice exhibited significantly decreased preference for the training object
559 when displaced, as indicated by the reduced discrimination index (**Figure 4B**), thus suggesting a
560 critical role of TIMP2 in spatial memory in healthy mice. We next employed contextual and cued
561 fear-conditioning to evaluate whether the mice differ in the ability to discriminate the previously
562 aversive training context or a new cue-drive context (**Figure 4C**). Assessment of context
563 discrimination revealed significantly reduced freezing behavior by TIMP2 KO mice, suggesting
564 impaired hippocampus-associated contextual discrimination in the absence of TIMP2 (**Figure 4D-**
565 **E**), while amygdala-associated cued freezing levels were unchanged (**Figure S2A**). We next
566 examined whether more complex hippocampus-dependent spatial memory was altered in a
567 Barnes maze assay in which mice use a variety of strategies while navigating an illuminated maze
568 surface to an escape hole using spatial cues. Strategies were divided into non-hippocampus-

569 dependent and hippocampus-dependent with increasing levels of cognitive demand (**Figure 4F**)
570 (Mateus-Pinheiro et al., 2017). Analysis of the strategies used to reach the escape hole revealed
571 that TIMP2 KO mice delayed the switch from non-hippocampal-dependent to hippocampal-
572 dependent strategies while performing the task (**Figure 4G**). On day 3 of the Barnes maze, a
573 significant lower proportion of TIMP2 KO mice used hippocampus-dependent strategies
574 compared to WT mice (**Figure 4H**). Further categorization of cognitive performance by scoring
575 the different strategies according to level of complexity related to spatial learning (Illouz et al.,
576 2016) showed that TIMP2 KO mice achieved significantly lower cognitive scores relative to WT
577 mice (**Figure 4I**), consistent with impaired hippocampus-dependent function in TIMP2 KO mice
578 while performing in the Barnes maze.

579 Importantly, we did not detect differences in motor function and overall activity in TIMP2
580 KO mice (**Figure S2B-J**). Motor coordination perturbations have been reported in TIMP2 mutant
581 mice (Jaworski et al., 2006), so we subjected the mice to a wide battery of motor function,
582 coordination, and activity assays, including rotarod, open field, wire testing, pole testing, grip
583 strength, none of which revealed changes in corresponding function between TIMP2 KO and WT
584 mice (**Figure S2B-I**). We detected impaired clasping behavior in TIMP2 KO relative to WT mice
585 (**Figure S2J**), as previously reported (Jaworski et al., 2006), but this form of motor coordination
586 does not impact performance observed for TIMP2 KO mice in the wide range of hippocampus-
587 dependent tasks utilized. No differences in anxiety-related behaviors in the open field were
588 observed between WT and TIMP2 KO mice (**Figure S2F**). Collectively, these results indicate a
589 critical role for TIMP2 in regulation of hippocampus-dependent memory.

590

591 **TIMP2 ablation leads to accumulation of ECM in the hippocampus**

592 We next investigated potential mechanisms that may account for how spine formation and adult
593 DG neurogenesis are regulated by TIMP2. Outside the brain, TIMP2 has been characterized to
594 be involved in ECM degradation and remodeling through its canonical binding partner MMP2

595 (Caterina et al., 2000; Wang et al., 2000). Brain ECM is dynamic, and accumulating evidence
596 suggests a role for ECM and its components in the regulation of synaptic plasticity, including in
597 spine remodeling (Magnowska et al., 2016; Nguyen et al., 2020), adult neurogenesis (Yamada et
598 al., 2018), and cognition (Yamada et al., 2018). We first assessed the levels of pro-MMP2 in
599 lysates of hippocampi from TIMP2 KO and WT mice. Interestingly, we found significantly elevated
600 levels of MMP2, both at the gene (**Figure 5A**) and protein (**Figure 5B-C**) levels in the absence of
601 TIMP2, reflecting an accumulation in response to loss in TIMP2 signaling and pointing to a
602 potential disruption in ECM remodeling and turnover in hippocampus.

603 In the brain, chondroitin sulfate proteoglycans (CSPGs) are the major class of ECM
604 proteins (Miyata et al., 2018; Zimmermann and Dours-Zimmermann, 2008). Particularly, the
605 proteoglycan aggrecan is a core CSPG expressed in perineuronal nets in the brain and highly
606 enriched in the ECM of the DG (Rowlands et al., 2018) that has been linked to synaptic plasticity
607 (Fawcett et al., 2019) and memory (Gogolla et al., 2009; Romberg et al., 2013). We therefore
608 analyzed aggrecan distribution in the hippocampus of WT and TIMP2 KO mice. Using super-
609 resolution confocal imaging in brain sections isolated from TIMP2 KO and WT mice, we found
610 that TIMP2 KO mice exhibited a significant increase in the density of aggrecan puncta in the DG
611 molecular layer (**Figure 5D-E**), the same area where we observed impaired spine remodeling in
612 TIMP2 KO relative to WT mice (**Figure 3**). To further determine if TIMP2 remodeling of the ECM
613 could affect accumulation of ECM near synapses given the synaptic deficits we observed in these
614 neurons, we analyzed aggrecan colocalization with the postsynaptic protein Homer1. We
615 observed that the DG of TIMP2 KO mice exhibited significantly increased colocalization of
616 Aggrecan with Homer1 relative to that observed in WT DG (**Figure 5F-G**). These data indicate
617 that TIMP2 normally promotes ECM remodeling and limits its deposition near synapses.

618 We next further characterized the relationship between TIMP2's effect on ECM and adult
619 neurogenesis, considering the known roles of ECM and its related components in the regulation
620 of proliferation and migration of newborn neurons [reviewed in (Cope and Gould, 2019)]. To

621 explore this possibility, we evaluated the migration of newborn neurons toward the molecular layer
622 by examining the distribution of DCX^+ immature neuroblasts in the SGZ relative to that in the GCL
623 of the DG. This analysis revealed significantly decreased distribution of DCX^+ immature neurons
624 in the GCL of TIMP2 KO mice (**Figure 5H-I**), reflecting a process whereby migration of newborn
625 neurons within the DG is apparently impaired in the absence of TIMP2. These data suggest that
626 the absence of TIMP2 leads to a tighter ECM structural environment that acts to spatially restrict
627 the migration of newborn neurons and plasticity of synapses, thus affecting overall adult
628 neurogenesis and spine dynamics. In support of this concept, we measured structural changes in
629 the ECM of TIMP2 KO mice by performing surface scanning electron microscopy (SEM) on
630 decellularized brains isolated from TIMP2 KO and WT mice. Interestingly, we detected altered
631 ECM microarchitecture in the form of thicker ECM fibers (**Figure 5J-K**) in hippocampi from TIMP2
632 KO compared to WT mice. Together, our results suggest that TIMP2 modulates the flexibility of
633 the ECM within the hippocampus to regulate plasticity processes, including adult neurogenesis
634 and spine plasticity.
635
636 **Creation of a conditional model to target neuronal pools of TIMP2**
637 To gain further mechanistic insight into TIMP2's role in the function of the hippocampus with
638 increased cellular resolution, we generated *Timp2*-floxed ($TIMP2^{fl/fl}$) mice using two-cell
639 homologous recombination (2C-HR)-CRISPR/Cas9-based genome editing. We inserted two
640 *loxP* sites flanking exon 2 of the *Timp2* gene transcript (**Figure 6A-B**) and then crossbred $Timp2^{fl/fl}$
641 mice with $Syn^{Cre/+}$ mice (**Figure 6C**) to specifically excise *Timp2* in neurons. Immunoblotting
642 against TIMP2 from isolated hippocampus lysates of $Syn^{Cre/+}$; $TIMP2^{fl/fl}$ or $TIMP2^{fl/fl}$ control mice
643 confirmed that conditional targeting of TIMP2 resulted in significantly reduced TIMP2 levels
644 compared to $TIMP2^{fl/fl}$ controls in hippocampus (**Figure 6D-E**). We performed further validation
645 by performing confocal microscopy in hippocampus of $Syn^{Cre/+}$; $TIMP2^{fl/fl}$ or $TIMP2^{fl/fl}$ control mice
646 to examine the cells in hippocampus expressing TIMP2. Quantification of $TIMP2^+$ $NeuN^+$ cells in

647 the hilus/DG, CA3 and CA1 regions revealed significant abrogation of TIMP2 in neurons upon its
648 conditional deletion (**Figure 6F-G**). These data validate our model as a tool for addressing the
649 role of neuronal TIMP2 in regulating the key cellular and behavioral phenotypes observed in the
650 context of global TIMP2 deletion.
651

652 **Neuronal TIMP2 regulation of the extracellular matrix regulates hippocampus-dependent**
653 **cognitive function and adult neurogenesis**

654 Given that we found that TIMP2 was expressed by neurons in DG and present at significant levels
655 in the extracellular space adjacent to these cells, we sought to determine whether the pool of
656 neuronal TIMP2 is specifically involved in hippocampus-dependent memory. Using the $Syn^{Cre/+}$;
657 $TIMP2^{fl/fl}$ mice we generated and validated (**Figure 6**), we created cohorts of $Syn^{Cre/+}$; $TIMP2^{fl/fl}$
658 mice and $TIMP2^{fl/fl}$ control littermates to evaluate performance in spatial memory tasks. We found
659 that $Syn^{Cre/+}$; $TIMP2^{fl/fl}$ mice exhibited significantly decreased preference for the displaced object
660 24 hours after training in the testing phase compared to $TIMP2^{fl/fl}$ controls, as indicated by a
661 reduced discrimination index in these mice (**Figure 7A**). Further assessment in the contextual
662 portion of fear-conditioning revealed a significant reduction in freezing levels by $Syn^{Cre/+}$; $TIMP2^{fl/fl}$
663 mice compared to $TIMP2^{fl/fl}$ controls, suggesting impaired contextual memory in the absence of
664 neuronal TIMP2 (**Figure 7B-C**). Cued freezing levels were indistinguishable between the groups
665 of mice (**Figure S3A**). We then subjected the mice to Barnes maze testing to examine
666 performance in search strategies to find the escape hole. Our search strategy analysis showed
667 that a smaller proportion of $Syn^{Cre/+}$; $TIMP2^{fl/fl}$ mice used hippocampus-dependent strategies
668 compared to $TIMP2^{fl/fl}$ mice (**Figure 7D-E**). Scoring their search strategy utilization by complexity
669 shows that $Syn^{Cre/+}$; $TIMP2^{fl/fl}$ mice score lower than their $TIMP2^{fl/fl}$ counterparts (**Figure 7F**),
670 suggesting TIMP2 from neurons is required for normal hippocampus-related memory and
671 learning. Importantly, we did not detect differences in overall motor function in terms of
672 coordination (**Figure S3B-C**), overall activity in the open field (**Figure S3D-E**), grip strength or

673 motor learning (**Figure S3G-I**) and clasping behavior (**Figure S3J**) in $Syn^{Cre/+}$; $TIMP2^{fl/fl}$ mice
674 relative to $TIMP2^{fl/fl}$ mice. No differences in anxiety-related behaviors in the open field were
675 observed between $TIMP2^{fl/fl}$ and $Syn^{Cre/+}$; $TIMP2^{fl/fl}$ mice (**Figure S3F**).

676 To test whether the local pool of neuronal TIMP2 affects the survival of newly generated
677 neurons, we analyzed the pool of $BrdU^+$ $NeuN^+$ cells after pulse-chase labeling with BrdU, as
678 described earlier (**Figure 2B**). Indeed, we observed that the deletion of TIMP2 within neurons
679 resulted in a significant decrease in the number of $BrdU^+$ $NeuN^+$ newborn neurons compared to
680 $TIMP2^{fl/fl}$ controls (**Figure 7G-H**).

681 To probe potential mechanisms by which TIMP2 expressed locally from neurons affects
682 hippocampus-dependent memory and adult neurogenesis, we next addressed ECM-related
683 remodeling in the DG of $Syn^{Cre/+}$; $TIMP2^{fl/fl}$ mice. TIMP2 deletion in neurons in $Syn^{Cre/+}$; $TIMP2^{fl/fl}$
684 mice resulted in a significant increase in the density of aggrecan-positive puncta compared to
685 $TIMP2^{fl/fl}$ controls (**Figure 7I-J**), as well as increased colocalization of Aggrecan with Homer1
686 (**Figure 7I, 7K**), consistent with an accumulation of ECM components adjacent to synapses, as
687 observed earlier. Together, our results show that the pool of neuronal TIMP2 is necessary to
688 promote ECM remodeling to enable synaptic plasticity and adult neurogenesis to facilitate normal
689 hippocampus-dependent memory.

690

691 **Discussion**

692 Our study provides an overview of how alterations in the ECM within the hippocampus by TIMP2
693 can directly regulate features of plasticity, including dendritic spine plasticity, adult neurogenesis
694 and hippocampus-dependent memory. We find that TIMP2 is highly expressed in neurons within
695 hippocampus and expressed at high levels in the brain extracellular space. Its removal induces
696 structural synaptic changes and deficits in adult neurogenesis, as predicted from changes
697 observed at the transcriptomic level, both of which result in impairments in hippocampus-
698 dependent memory function. We demonstrate that TIMP2's role in ECM remodeling is associated

699 with changes in the flexibility of synaptic plasticity, impinging on processes like neuronal migration
700 and differentiation. We generate and characterize a novel mouse model for the conditional
701 deletion of TIMP2 within neurons in order to understand which phenotypes associated with TIMP2
702 can be attributed to the neuronal pool of TIMP2. We report that mice in which neuronal pools of
703 TIMP2 are targeted exhibited the major functional phenotypes observed in mice in which TIMP2
704 is deleted globally, highlighting molecular mechanisms through which neuronal TIMP2 promotes
705 synaptic plasticity through regulation in the ECM to facilitate normal memory.
706
707 **TIMP2 regulation of synaptic remodeling and adult neurogenesis**
708 The development and maintenance of synapses is critical in the establishment of functional
709 neuronal circuits, and emerging evidence indicates a role for the ECM and its components in
710 regulating synapse structure and morphology (Dansie and Ethell, 2011; Singhal and Martin,
711 2011). Few reports to date have shown that regulating the organization of the ECM is critical to
712 ensuring proper synaptic morphology (Kurshan et al., 2014). Herein, we show that the ECM
713 regulator TIMP2 is important for normal spine morphology in the hippocampus. These
714 observations are in line with previous *in vitro* reports that neurites of TIMP2 KO neurons are
715 significantly shorter than WT neurons (Perez-Martinez and Jaworski, 2005). We used high-
716 resolution imaging of labeled granule cells in the intact hippocampus of TIMP2 KO and WT mice
717 to show that TIMP2 regulates dendritic spine density, with a loss in KO mice in the class of spines
718 involved in memory, mushroom spines (Bourne and Harris, 2007). This finding is consistent with
719 reports that neutralization of TIMP2 leads to a dramatic loss in LTP (Castellano et al., 2017).
720 Moreover, when TIMP2 is targeted globally or specifically within neurons, ECM components like
721 aggrecan accumulate around synapses in the hippocampus and the ECM is more dense, based
722 on SEM data, suggesting that TIMP2 acts directly within the hippocampus to modulate plasticity
723 on a structural level. In agreement with its role in modulating plasticity, we also find that TIMP2
724 regulates the process of adult neurogenesis. While immature neuroblasts were unaltered in mice

725 with systemic modulation of TIMP2 in young mice (Castellano et al., 2017), presumably due to
726 the window over which TIMP2 was modulated being too short to reflect changes in DCX$^+$ cells,
727 we now show that removal of TIMP2, both globally and from neurons in the hippocampus, results
728 in disruption in adult neurogenesis, including in neural progenitor proliferation and maturation.
729 This is in line with sparse evidence *in vitro* indicating that TIMP2 expression was significantly
730 upregulated upon neuronal differentiation (Jaworski and Perez-Martinez, 2006), and that it may
731 be involved in differentiation (Perez-Martinez and Jaworski, 2005). Intriguingly, we observed that
732 TIMP2 deletion affected the migration of immature DCX$^+$ neurons towards the molecular layer,
733 arguing for a role of ECM in regulating neuronal migration (Wang et al., 2018). It has been
734 documented that ECM molecules participate in neurogenesis (Cope and Gould, 2019), though
735 the mechanisms by which they regulate neuronal differentiation are still limited. CSPGs are known
736 to surround new neurons in the hippocampus, and have recently been shown to be important in
737 the production of new neurons (Yamada et al., 2018). Moreover, ECM-related proteins, such as
738 reelin, have been shown to play critical roles in neuronal migration (Wang et al., 2018).
739
740 **Roles of TIMP2 remodeling of the ECM within hippocampus**
741 The molecular details regarding how molecules like TIMP2 may interact with the ECM to alter
742 functional plasticity remain unclear. TIMP2 is traditionally recognized for its unique dual role in
743 regulating both the activation of pro-MMP2 and the inhibition of MMP2 activity necessary for ECM
744 remodeling (Caterina et al., 2000; Wang et al., 2000). We observed that the deletion of TIMP2
745 leads to increased levels of *Mmp2* and pro-MMP2 levels within hippocampus, perhaps reflecting
746 compensatory responses to reduced TIMP2 and impaired MMP2 activation, as described outside
747 of the brain (Caterina et al., 2000; Wang et al., 2000). The accumulated pro-MMP2 appears to
748 translate to less remodeling of the ECM and its resulting accumulation around cells in the DG
749 neurogenic cells that we observe. A proposed mechanism of spine stabilization and remodeling
750 by ECM includes a structural spatial restriction mechanism in which ECM components, including

751 CSPGs, form a matrix around dendritic spines to provide extracellular rigidity and physically
752 restrict spine motion (Levy et al., 2014). MMPs themselves can modulate structural plasticity by
753 loosening the ECM structure, allowing for a more permissive environment (Cope and Gould,
754 2019). Moreover, stiffness of the surrounding environment determined by ECM complexity has
755 been shown to regulate cell migration (Choi et al., 2012; Vincent et al., 2013), including for neural
756 stem cell proliferation, differentiation, and migration *in vitro* (Leipzig and Shoichet, 2009;
757 Rammensee et al., 2017; Saha et al., 2008). This modulation has been proposed to be among
758 fundamental cell fate-determining factors in neural development and neurological disorders
759 (Barnes et al., 2017; Hall et al., 2021; Javier-Torrent et al., 2021). Our results argue that, in the
760 absence of TIMP2, ECM accumulation leads to a denser network that creates physical restrictions
761 that impact the turnover of synapses from thin into mature mushroom-shaped spines, while
762 impeding the proliferation and migration or cells related to the process of adult neurogenesis.
763
764 **TIMP2 regulates functional effects exerted by the hippocampus**
765 In line with reports implicating disrupted synaptic plasticity and neurogenesis in cognitive
766 dysfunction (Cope and Gould, 2019), we show how TIMP2 deletion affects hippocampus
767 plasticity, ultimately causing striking memory impairment. Both global and neuron-specific
768 targeting of TIMP2 levels leads to deficits in hippocampus-dependent memory tasks, mimicking
769 previously described phenotypes observed upon systemic targeting of TIMP2 in aging (Castellano
770 et al., 2017). Our results strongly reinforce a surprising link among TIMP2, synaptic plasticity, and
771 memory in the healthy hippocampus. Our data support the concept that TIMP2 regulates spine
772 dynamics and neurogenesis, which are important for memory. Importantly, the cognitive
773 phenotypes described here cannot be attributed to TIMP2's role in other brain regions related to
774 motor function, though earlier work in younger mice described subtle deficits in coordination upon
775 TIMP2 deletion (Jaworski et al., 2006), primarily related to cerebellar alterations deletion
776 (Jaworski et al., 2006). We show that TIMP2-mediated roles in ECM to regulate cellular

phenotypes are associated with changes in MMP2. TIMP2 likely interacts with many MMPs and other binding partner to mediate functional changes under different conditions. Others have shown that TIMP2 exerts diverse biological functions in addition to MMP2. Through its binding of alpha3beta1 integrin, TIMP2 has been shown to regulate cell cycle progression in PC12 cells, independent of MMP inhibitory activity (Perez-Martinez and Jaworski, 2005). It is possible that TIMP2 exerts its diverse biological functions through interactions with different binding partners, or that it exerts its activities differently *in vivo* versus *in vitro*, all of which will need to be further explored in future studies. Moreover, while we mostly find TIMP2 expressed in neurons in our study, TIMP2 expression from other cell types may be important in certain pathological contexts (Keren-Shaul et al., 2017) that could be important to explore further, especially as a role for microglia in remodeling the ECM to promote synapse plasticity in the hippocampus has been recently described (Nguyen et al., 2020).

TIMP2 function in physiology, aging and pathology

Dysregulation of the ECM is implicated in cognitive dysfunction that occurs in aging (Birch, 2018) and in disease (Sun et al., 2021). The progressive decline in TIMP2 expression with age (Castellano et al., 2017) occurs in parallel with deficits in memory (Bettio et al., 2017) and ECM accumulation (Vegh et al., 2014b), while systemic treatment with TIMP2 revitalizes hippocampus-related function in aged mice (Castellano et al., 2017). Moreover, ECM clearance is beneficial in mouse models of Alzheimer's disease pathology (Vegh et al., 2014a). It has been increasingly appreciated that adult neurogenesis in the human DG is dysregulated in Alzheimer's disease brain (Moreno-Jimenez et al., 2019), in addition to the loss observed in dendritic spine integrity. Therefore, defining the precise molecular mechanisms accounting for how TIMP2 regulates synaptic plasticity within the hippocampus in the healthy brain may lead to the development of novel approaches for cognitive repair in contexts of aging or neurodegeneration.

803 **Acknowledgments**

804 We gratefully acknowledge the contributions of the Mouse Genetics and Gene Targeting (MGGT)
805 CoRE facility (Kevin Kelley, ISMMS), which is supported by ISMMS and the National Cancer
806 Institute of the NIH under award P30CA196521, for two-cell stage embryo microinjections for
807 generating TIMP2$^{fl/fl}$ mice. We also thank Chingwen Yang of the CRISPR and Genome Editing
808 Center (Rockefeller University) for assistance generating constructs to develop the TIMP2$^{fl/fl}$ line.
809 We thank Yihang Wang (ISMMS) for RNA isolation support, Nikos Tzavaras and Deanna Benson
810 of the Microscopy CoRE and Advanced Bioimaging Center (ISMMS) for advice and equipment
811 for Airyscan microscopy and image analysis, Lee Cohen-Gould of the Electron Microscopy &
812 Histology Services of Weill Cornell Medicine Microscopy & Image Analysis Core for SEM sample
813 preparation, Jorge Morales of the Microscopy Facility (CCNY) for SEM acquisition support, and
814 Ron Gordon and Andy Leonard of the EM Core (ISMMS) for advice and sample preparation for
815 SEM. This work was funded by the National Institute on Aging (R01AG061382 (J.M.C),
816 RF1AG072300 (J.M.C.), T32AG049688 (B.M.H.), and R01AG061382-02S1 (J.M.C., S.M.P)).

817 **Author contributions**

818 A.C.F. and J.M.C. conceived and designed the experiments, performed data analysis and
819 interpretation, and wrote the manuscript. A.C.F. conducted the experiments. B.M.H. performed
820 and analyzed microdialysis experiments. S.M.P analyzed data for RNAseq experiments. H. L.
821 and J.D.Z performed or analyzed motor or Barnes maze experiments. M.V. performed intracellular
822 dye injections for spine labeling, and analyzed/interpreted data with P.R.H. T.K. and T.A. assisted
823 with design and analysis of TIMP2$^{fl/fl}$ validation data. All authors approved the final manuscript.
824

825 **Declaration of interests**

826 J.M.C. is listed as a co-inventor on patents for treating aging-associated conditions, including the
827 use of young plasma administration (US10688130B2) or youth-associated protein TIMP2
828 (US10617744B2), the latter of which is licensed to Alkahest, Inc.

829

830 **References**

831 Anacker, C., and Hen, R. (2017). Adult hippocampal neurogenesis and cognitive flexibility
832 - linking memory and mood. Nature reviews Neuroscience *18*, 335-346.

833 Barnes, J.M., Przybyla, L., and Weaver, V.M. (2017). Tissue mechanics regulate brain
834 development, homeostasis and disease. J Cell Sci *130*, 71-82.

835 Bettio, L.E.B., Rajendran, L., and Gil-Mohapel, J. (2017). The effects of aging in the
836 hippocampus and cognitive decline. Neurosci Biobehav Rev *79*, 66-86.

837 Birch, H.L. (2018). Extracellular Matrix and Ageing. Subcell Biochem *90*, 169-190.

838 Bourne, J., and Harris, K.M. (2007). Do thin spines learn to be mushroom spines that
839 remember? Curr Opin Neurobiol *17*, 381-386.

840 Brew, K., and Nagase, H. (2010). The tissue inhibitors of metalloproteinases (TIMPs): an
841 ancient family with structural and functional diversity. Biochimica et biophysica acta *1803*,
842 55-71.

843 Castellano, J.M., Kim, J., Stewart, F.R., Jiang, H., DeMattos, R.B., Patterson, B.W.,
844 Fagan, A.M., Morris, J.C., Mawuenyega, K.G., Cruchaga, C.*, et al.* (2011). Human apoE
845 isoforms differentially regulate brain amyloid-beta peptide clearance. Sci Transl Med *3*,
846 89ra57.

847 Castellano, J.M., Mosher, K.I., Abbey, R.J., McBride, A.A., James, M.L., Berdnik, D.,
848 Shen, J.C., Zou, B., Xie, X.S., Tingle, M.*, et al.* (2017). Human umbilical cord plasma
849 proteins revitalize hippocampal function in aged mice. Nature *544*, 488-492.

850 Caterina, J.J., Yamada, S., Caterina, N.C., Longenecker, G., Holmback, K., Shi, J.,
851 Yermovsky, A.E., Engler, J.A., and Birkedal-Hansen, H. (2000). Inactivating mutation of
852 the mouse tissue inhibitor of metalloproteinases-2(Timp-2) gene alters proMMP-2
853 activation. The Journal of biological chemistry *275*, 26416-26422.

854 Choi, Y.S., Vincent, L.G., Lee, A.R., Kretchmer, K.C., Chirasatitsin, S., Dobke, M.K., and
855 Engler, A.J. (2012). The alignment and fusion assembly of adipose-derived stem cells on
856 mechanically patterned matrices. Biomaterials *33*, 6943-6951.

857 Cope, E.C., and Gould, E. (2019). Adult Neurogenesis, Glia, and the Extracellular Matrix.
858 Cell Stem Cell *24*, 690-705.

859 Dansie, L.E., and Ethell, I.M. (2011). Casting a net on dendritic spines: the extracellular
860 matrix and its receptors. Dev Neurobiol *71*, 956-981.

861 De Waele, J., Reekmans, K., Daans, J., Goossens, H., Berneman, Z., and Ponsaerts, P.
862 (2015). 3D culture of murine neural stem cells on decellularized mouse brain sections.
863 Biomaterials *41*, 122-131.

864 Dewing, J.M., Carare, R.O., Lotery, A.J., and Ratnayaka, J.A. (2019). The Diverse Roles
865 of TIMP-3: Insights into Degenerative Diseases of the Senescent Retina and Brain. Cells
866 *9*.

867 Dickstein, D.L., Dickstein, D.R., Janssen, W.G.M., Hof, P.R., Glaser, J.R., Rodriguez, A.,
868 O'Connor, N., Angstman, P., and Tappan, S.J. (2016). Automatic Dendritic Spine
869 Quantification from Confocal Data with Neurolucida 360. Curr Protoc Neurosci *77*, 1 27
870 21-21 27 21.

871 Fager, N., and Jaworski, D.M. (2000). Differential spatial distribution and temporal
872 regulation of tissue inhibitor of metalloproteinase mRNA expression during rat central
873 nervous system development. Mech Dev *98*, 105-109.

874 Fawcett, J.W., Oohashi, T., and Pizzorusso, T. (2019). The roles of perineuronal nets and
875 the perinodal extracellular matrix in neuronal function. Nature reviews Neuroscience *20*,
876 451-465.

877 Gogolla, N., Caroni, P., Luthi, A., and Herry, C. (2009). Perineuronal nets protect fear
878 memories from erasure. Science *325*, 1258-1261.

879 Gu, B., Posfai, E., and Rossant, J. (2018). Efficient generation of targeted large insertions
880 by microinjection into two-cell-stage mouse embryos. Nat Biotechnol *36*, 632-637.

881 Guo, T., Hao, H., Zhou, L., Zhou, F., and Yu, D. (2018). Association of SNPs in the TIMP-
882 2 gene and large artery atherosclerotic stroke in southern Chinese Han population.
883 Oncotarget *9*, 4698-4706.

884 Hall, C.M., Moeendarbary, E., and Sheridan, G.K. (2021). Mechanobiology of the brain in
885 ageing and Alzheimer's disease. Eur J Neurosci *53*, 3851-3878.

886 Illouz, T., Madar, R., Louzoun, Y., Griffioen, K.J., and Okun, E. (2016). Unraveling
887 cognitive traits using the Morris water maze unbiased strategy classification (MUST-C)
888 algorithm. Brain Behav Immun *52*, 132-144.

889 Ippolito, D.M., and Eroglu, C. (2010). Quantifying synapses: an immunocytochemistry-
890 based assay to quantify synapse number. J Vis Exp.

891 Javier-Torrent, M., Zimmer-Bensch, G., and Nguyen, L. (2021). Mechanical Forces
892 Orchestrate Brain Development. Trends Neurosci *44*, 110-121.

893 Jaworski, D.M., and Perez-Martinez, L. (2006). Tissue inhibitor of metalloproteinase-2
894 (TIMP-2) expression is regulated by multiple neural differentiation signals. J Neurochem
895 *98*, 234-247.

896 Jaworski, D.M., Soloway, P., Caterina, J., and Falls, W.A. (2006). Tissue inhibitor of
897 metalloproteinase-2(TIMP-2)-deficient mice display motor deficits. J Neurobiol *66*, 82-94.

898 Jedlicka, P., Vlachos, A., Schwarzacher, S.W., and Deller, T. (2008). A role for the spine
899 apparatus in LTP and spatial learning. Behav Brain Res *192*, 12-19.

900 Kaczorowska, A., Miekus, N., Stefanowicz, J., and Adamkiewicz-Drozynska, E. (2020).
901 Selected Matrix Metalloproteinases (MMP-2, MMP-7) and Their Inhibitor (TIMP-2) in Adult
902 and Pediatric Cancer. Diagnostics (Basel) *10*.

903 Kandalam, V., Basu, R., Moore, L., Fan, D., Wang, X., Jaworski, D.M., Oudit, G.Y., and
904 Kassiri, Z. (2011). Lack of tissue inhibitor of metalloproteinases 2 leads to exacerbated
905 left ventricular dysfunction and adverse extracellular matrix remodeling in response to
906 biomechanical stress. Circulation *124*, 2094-2105.

907 Katsimpardi, L., Litterman, N.K., Schein, P.A., Miller, C.M., Loffredo, F.S., Wojtkiewicz,
908 G.R., Chen, J.W., Lee, R.T., Wagers, A.J., and Rubin, L.L. (2014). Vascular and
909 neurogenic rejuvenation of the aging mouse brain by young systemic factors. Science
910 *344*, 630-634.

911 Keren-Shaul, H., Spinrad, A., Weiner, A., Matcovitch-Natan, O., Dvir-Szternfeld, R.,
912 Ulland, T.K., David, E., Baruch, K., Lara-Astaiso, D., Toth, B.*, et al.* (2017). A Unique
913 Microglia Type Associated with Restricting Development of Alzheimer's Disease. Cell
914 *169*, 1276-1290 e1217.

915 Kurshan, P.T., Phan, A.Q., Wang, G.J., Crane, M.M., Lu, H., and Shen, K. (2014).
916 Regulation of synaptic extracellular matrix composition is critical for proper synapse
917 morphology. The Journal of neuroscience : the official journal of the Society for
918 Neuroscience *34*, 12678-12689.

919 Leipzig, N.D., and Shoichet, M.S. (2009). The effect of substrate stiffness on adult neural
920 stem cell behavior. Biomaterials *30*, 6867-6878.

921 Levy, A.D., Omar, M.H., and Koleske, A.J. (2014). Extracellular matrix control of dendritic
922 spine and synapse structure and plasticity in adulthood. Front Neuroanat *8*, 116.

923 Magnowska, M., Gorkiewicz, T., Suska, A., Wawrzyniak, M., Rutkowska-Wlodarczyk, I.,
924 Kaczmarek, L., and Wlodarczyk, J. (2016). Transient ECM protease activity promotes
925 synaptic plasticity. Sci Rep *6*, 27757.

926 Mateus-Pinheiro, A., Alves, N.D., Patricio, P., Machado-Santos, A.R., Loureiro-Campos,
927 E., Silva, J.M., Sardinha, V.M., Reis, J., Schorle, H., Oliveira, J.F.*, et al.* (2017).
928 AP2gamma controls adult hippocampal neurogenesis and modulates cognitive, but not
929 anxiety or depressive-like behavior. Mol Psychiatry *22*, 1725-1734.

930 Miyata, S., Nadanaka, S., Igarashi, M., and Kitagawa, H. (2018). Structural Variation of
931 Chondroitin Sulfate Chains Contributes to the Molecular Heterogeneity of Perineuronal
932 Nets. Front Integr Neurosci *12*, 3.

933 Moreno-Jimenez, E.P., Flor-Garcia, M., Terreros-Roncal, J., Rabano, A., Cafini, F.,
934 Pallas-Bazarra, N., Avila, J., and Llorens-Martin, M. (2019). Adult hippocampal
935 neurogenesis is abundant in neurologically healthy subjects and drops sharply in patients
936 with Alzheimer's disease. Nat Med *25*, 554-560.

937 Moser, M.B., Trommald, M., and Andersen, P. (1994). An increase in dendritic spine
938 density on hippocampal CA1 pyramidal cells following spatial learning in adult rats
939 suggests the formation of new synapses. Proceedings of the National Academy of
940 Sciences of the United States of America *91*, 12673-12675.

941 Nguyen, P.T., Dorman, L.C., Pan, S., Vainchtein, I.D., Han, R.T., Nakao-Inoue, H.,
942 Taloma, S.E., Barron, J.J., Molofsky, A.B., Kheirbek, M.A.*, et al.* (2020). Microglial
943 Remodeling of the Extracellular Matrix Promotes Synapse Plasticity. Cell *182*, 388-403
944 e315.

945 Nicaise, A.M., Johnson, K.M., Willis, C.M., Guzzo, R.M., and Crocker, S.J. (2019). TIMP-
946 1 Promotes Oligodendrocyte Differentiation Through Receptor-Mediated Signaling. Mol
947 Neurobiol *56*, 3380-3392.

948 Perez-Martinez, L., and Jaworski, D.M. (2005). Tissue inhibitor of metalloproteinase-2
949 promotes neuronal differentiation by acting as an anti-mitogenic signal. The Journal of
950 neuroscience : the official journal of the Society for Neuroscience *25*, 4917-4929.

951 Price, K.A., Varghese, M., Sowa, A., Yuk, F., Brautigam, H., Ehrlich, M.E., and Dickstein,
952 D.L. (2014). Altered synaptic structure in the hippocampus in a mouse model of
953 Alzheimer's disease with soluble amyloid-beta oligomers and no plaque pathology. Mol
954 Neurodegener *9*, 41.

955 Rammensee, S., Kang, M.S., Georgiou, K., Kumar, S., and Schaffer, D.V. (2017).
956 Dynamics of Mechanosensitive Neural Stem Cell Differentiation. Stem cells *35*, 497-506.

957 Rodriguez, A., Ehlenberger, D.B., Dickstein, D.L., Hof, P.R., and Wearne, S.L. (2008).
958 Automated three-dimensional detection and shape classification of dendritic spines from
959 fluorescence microscopy images. PloS one *3*, e1997.

960 Romberg, C., Yang, S., Melani, R., Andrews, M.R., Horner, A.E., Spillantini, M.G.,
961 Bussey, T.J., Fawcett, J.W., Pizzorusso, T., and Saksida, L.M. (2013). Depletion of
962 perineuronal nets enhances recognition memory and long-term depression in the
963 perirhinal cortex. The Journal of neuroscience : the official journal of the Society for
964 Neuroscience *33*, 7057-7065.

965 Rowlands, D., Lensjo, K.K., Dinh, T., Yang, S., Andrews, M.R., Hafting, T., Fyhn, M.,
966 Fawcett, J.W., and Dick, G. (2018). Aggrecan Directs Extracellular Matrix-Mediated
967 Neuronal Plasticity. The Journal of neuroscience : the official journal of the Society for
968 Neuroscience *38*, 10102-10113.

969 Saha, K., Keung, A.J., Irwin, E.F., Li, Y., Little, L., Schaffer, D.V., and Healy, K.E. (2008).
970 Substrate modulus directs neural stem cell behavior. Biophys J *95*, 4426-4438.

971 Singhal, N., and Martin, P.T. (2011). Role of extracellular matrix proteins and their
972 receptors in the development of the vertebrate neuromuscular junction. Dev Neurobiol
973 *71*, 982-1005.

974 Solga, R., Behrens, J., Ziemann, A., Riou, A., Berwanger, C., Becker, L., Garrett, L., de
975 Angelis, M.H., Fischer, L., Coras, R.*, et al.* (2019). CRN2 binds to TIMP4 and MMP14
976 and promotes perivascular invasion of glioblastoma cells. Eur J Cell Biol *98*, 151046.

977 Sun, Y., Xu, S., Jiang, M., Liu, X., Yang, L., Bai, Z., and Yang, Q. (2021). Role of the
978 Extracellular Matrix in Alzheimer's Disease. Front Aging Neurosci *13*, 707466.

979 Tajerian, M., Hung, V., Nguyen, H., Lee, G., Joubert, L.M., Malkovskiy, A.V., Zou, B., Xie,
980 S., Huang, T.T., and Clark, J.D. (2018). The hippocampal extracellular matrix regulates
981 pain and memory after injury. Mol Psychiatry *23*, 2302-2313.

982 Takeshita, H., Yamamoto, K., Nozato, S., Inagaki, T., Tsuchimochi, H., Shirai, M.,
983 Yamamoto, R., Imaizumi, Y., Hongyo, K., Yokoyama, S.*, et al.* (2017). Modified forelimb
984 grip strength test detects aging-associated physiological decline in skeletal muscle
985 function in male mice. Sci Rep *7*, 42323.

986 Ulrich, J.D., Burchett, J.M., Restivo, J.L., Schuler, D.R., Verghese, P.B., Mahan, T.E.,
987 Landreth, G.E., Castellano, J.M., Jiang, H., Cirrito, J.R.*, et al.* (2013). In vivo
988 measurement of apolipoprotein E from the brain interstitial fluid using microdialysis. Mol
989 Neurodegener *8*, 13.

990 Vegh, M.J., Heldring, C.M., Kamphuis, W., Hijazi, S., Timmerman, A.J., Li, K.W., van
991 Nierop, P., Mansvelder, H.D., Hol, E.M., Smit, A.B.*, et al.* (2014a). Reducing hippocampal

992 extracellular matrix reverses early memory deficits in a mouse model of Alzheimer's
993 disease. Acta Neuropathol Commun *2*, 76.

994 Vegh, M.J., Rausell, A., Loos, M., Heldring, C.M., Jurkowski, W., van Nierop, P.,
995 Paliukhovich, I., Li, K.W., del Sol, A., Smit, A.B.*, et al.* (2014b). Hippocampal extracellular
996 matrix levels and stochasticity in synaptic protein expression increase with age and are
997 associated with age-dependent cognitive decline. Mol Cell Proteomics *13*, 2975-2985.

998 Villeda, S.A., Luo, J., Mosher, K.I., Zou, B., Britschgi, M., Bieri, G., Stan, T.M., Fainberg,
999 N., Ding, Z., Eggel, A.*, et al.* (2011). The ageing systemic milieu negatively regulates
1000 neurogenesis and cognitive function. Nature *477*, 90-94.

1001 Villeda, S.A., Plambeck, K.E., Middeldorp, J., Castellano, J.M., Mosher, K.I., Luo, J.,
1002 Smith, L.K., Bieri, G., Lin, K., Berdnik, D.*, et al.* (2014). Young blood reverses age-related
1003 impairments in cognitive function and synaptic plasticity in mice. Nat Med *20*, 659-663.

1004 Vincent, L.G., Choi, Y.S., Alonso-Latorre, B., del Alamo, J.C., and Engler, A.J. (2013).
1005 Mesenchymal stem cell durotaxis depends on substrate stiffness gradient strength.
1006 Biotechnol J *8*, 472-484.

1007 Wang, S., Brunne, B., Zhao, S., Chai, X., Li, J., Lau, J., Failla, A.V., Zobiak, B., Sibbe, M.,
1008 Westbrook, G.L.*, et al.* (2018). Trajectory Analysis Unveils Reelin's Role in the Directed
1009 Migration of Granule Cells in the Dentate Gyrus. The Journal of neuroscience : the official
1010 journal of the Society for Neuroscience *38*, 137-148.

1011 Wang, Z., Juttermann, R., and Soloway, P.D. (2000). TIMP-2 is required for efficient
1012 activation of proMMP-2 in vivo. The Journal of biological chemistry *275*, 26411-26415.

1013 Yamada, J., Nadanaka, S., Kitagawa, H., Takeuchi, K., and Jinno, S. (2018). Increased
1014 Synthesis of Chondroitin Sulfate Proteoglycan Promotes Adult Hippocampal
1015 Neurogenesis in Response to Enriched Environment. The Journal of neuroscience : the
1016 official journal of the Society for Neuroscience *38*, 8496-8513.

1017 Yang, G., Pan, F., and Gan, W.B. (2009). Stably maintained dendritic spines are
1018 associated with lifelong memories. Nature *462*, 920-924.

1019 Zhu, J.W., Li, Y.F., Wang, Z.T., Jia, W.Q., and Xu, R.X. (2016). Toll-Like Receptor 4
1020 Deficiency Impairs Motor Coordination. Front Neurosci *10*, 33.

1021 Zhu, Y., Romero, M.I., Ghosh, P., Ye, Z., Charnay, P., Rushing, E.J., Marth, J.D., and
1022 Parada, L.F. (2001). Ablation of NF1 function in neurons induces abnormal development
1023 of cerebral cortex and reactive gliosis in the brain. Genes Dev *15*, 859-876.

1024 Zimmermann, D.R., and Dours-Zimmermann, M.T. (2008). Extracellular matrix of the
1025 central nervous system: from neglect to challenge. Histochem Cell Biol *130*, 635-653.

1026 Zuo, Y., Lin, A., Chang, P., and Gan, W.B. (2005). Development of long-term dendritic
1027 spine stability in diverse regions of cerebral cortex. Neuron *46*, 181-189.

1028

1029

1030 **Figure 1**

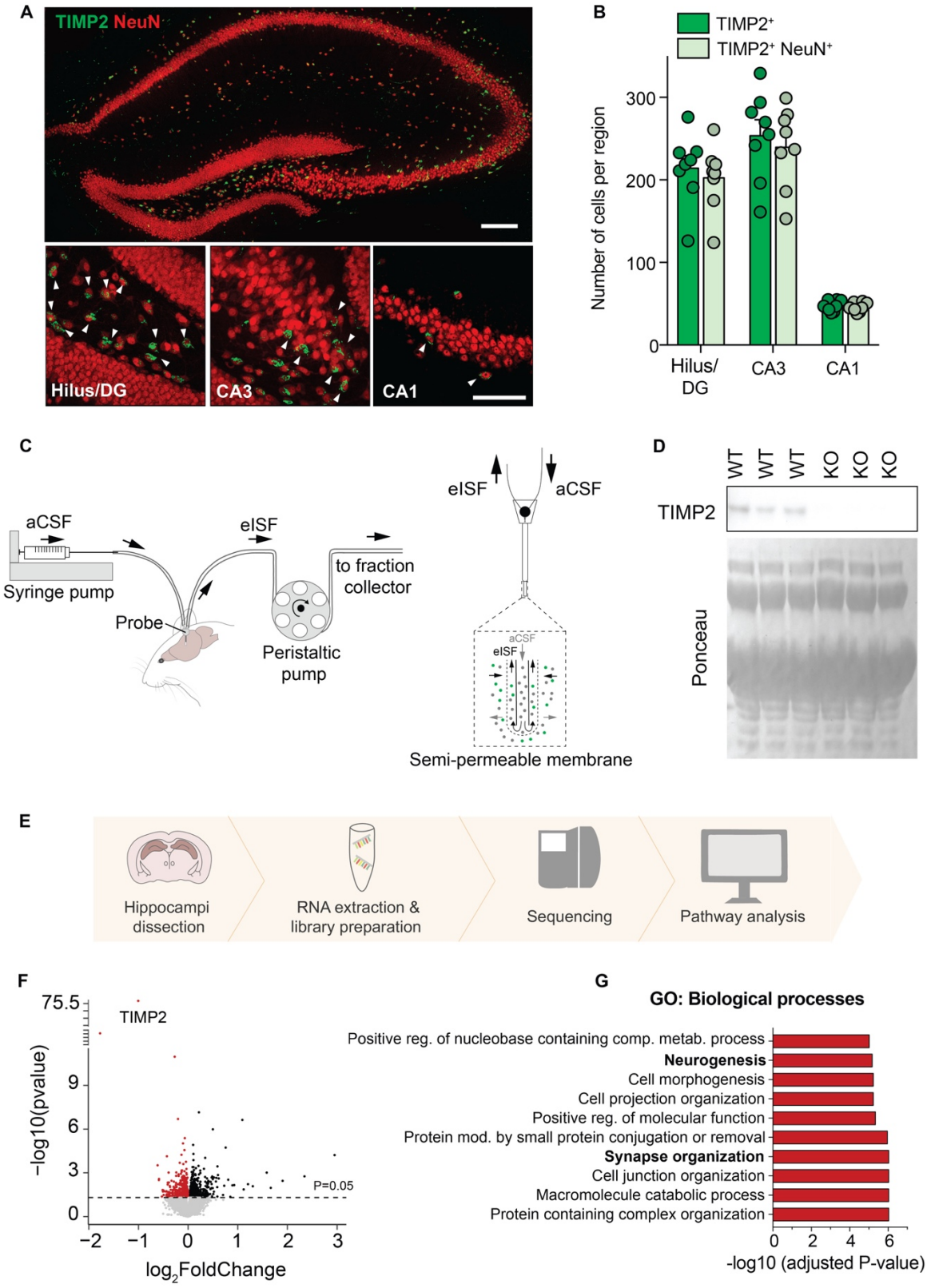

1031 **Figure 1. TIMP2 is expressed in neurons of the hippocampus, and its deletion induces**
1032 **transcriptomic changes**. **(A)** Low-magnification view (upper image) of mouse hippocampus and
1033 high-magnification view (lower images) of hilus/DG, CA3, and CA1 subregions showing $TIMP2^+$
1034 and $TIMP2^+$ $NeuN^+$ cells. Scale bars, 200 μm and 20 μm (inset). **(B)** Quantification of the total
1035 number of $TIMP2^+$ cells and $TIMP2^+$ $NeuN^+$ cells across hippocampal subregions in WT mice (2
1036 months of age; N = 8, males and females). **(C)** Schematic representation of high molecular-weight
1037 cut-off (1-MDa) *in vivo* microdialysis to assay TIMP2 levels in mouse hippocampal ISF. **(D)** TIMP2
1038 immunoblotting of hippocampal ISF dialyzed from 2-month-old WT and TIMP2 KO mice, with
1039 corresponding Ponceau S stain. **(E)** Schematic representation of bulk RNA-seq workflow
1040 performed in isolated WT and TIMP2 KO hippocampi (N=13-17/group, sex-matched) for
1041 transcriptomic analysis. **(F)** Volcano plot showing the fold-change of genes ($\log_2$ scale)
1042 differentially expressed in hippocampus of TIMP2 KO vs. WT mice. Downregulated DEGs at $P <$
1043 0.05 are highlighted in red (upregulated in black). **(G)** Top 10 significant pathways for
1044 downregulated DEGs from Gene Set Enrichment Analysis. Data are represented as mean ± SEM.
1045 DG, dentate gyrus; eISF, exchangeable interstitial fluid; aCSF, artificial cerebrospinal fluid.
1046

1047 **Figure 2.**
1048

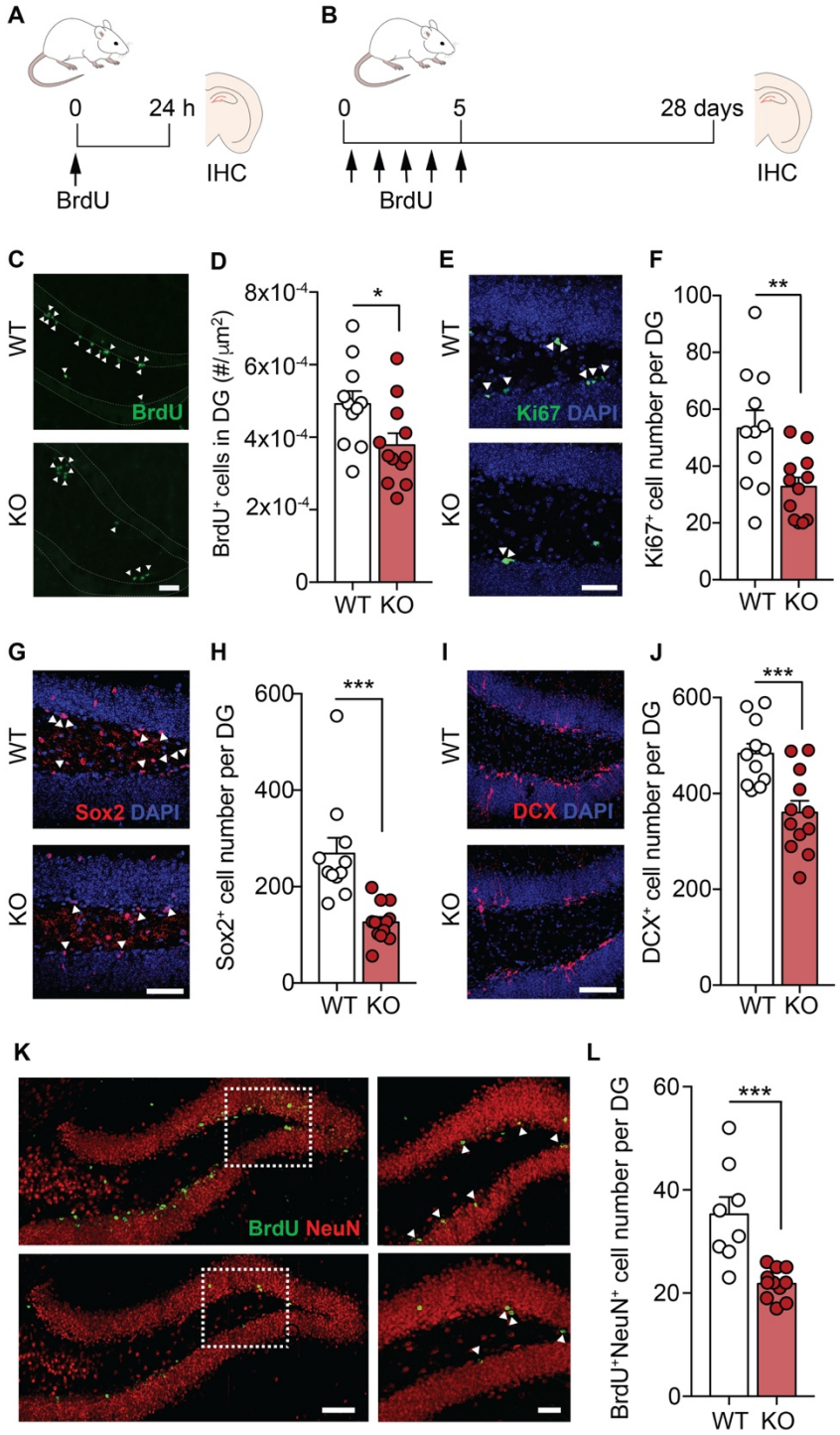

1049 **Figure 2. TIMP2 is necessary for adult neurogenesis in the normal dentate gyrus**

1050 **(A)** Schematic timeline of BrdU intraperitoneal injection protocol to label proliferating cells in the
1051 DG in isolated brain sections. **(B)** Schematic timeline of BrdU intraperitoneal injection protocol
1052 used for cell fate "survival" labeling in DG of isolated brain sections. **(C)** Representative confocal
1053 microscopy images of $BrdU^+$ cells in the DG of WT and TIMP2 KO mice (2-3 months of age, N =
1054 11-12 mice per group; arrowheads indicate $BrdU^+$ cells; scale bar, 50 μm) with corresponding **(D)**
1055 quantification of number of $BrdU^+$ cells in the dentate gyrus per unit area. **(E)** Representative
1056 confocal microscopy images of proliferating $Ki67^+$ cells in the DG of WT and TIMP2 KO mice (2-
1057 3 months of age, N = 11-12 mice per group; arrowheads indicate $Ki67^+$ cells; scale bar, 50 μm)
1058 with corresponding **(F)** quantification of the number of $Ki67^+$ proliferating cells per DG in WT and
1059 TIMP2 KO mice. **(G)** Representative confocal microscopy images of $Sox2^+$ in the DG of WT and
1060 TIMP2 KO mice (2-3 months of age, N = 11-12 mice per group; arrowheads indicate $Sox2^+$ cells;
1061 scale bar, 50 μm) with corresponding **(H)** quantification of $Sox2^+$ neural progenitor cells in the DG
1062 of WT and TIMP2 KO mice. **(I)** Representative confocal microscopy images of DCX^+ cells in the
1063 DG of WT and TIMP2 KO mice (2-3 months of age, N = 11-12 mice per group; scale bar, 50 μm)
1064 with corresponding **(J)** quantification of DCX^+ immature neuroblasts in DG of WT and TIMP2 KO
1065 mice. **(K)** Representative confocal microscopy images of $BrdU^+$ $NeuN^+$ cells in DG of WT and
1066 TIMP2 KO mice (2-3 months of age. N = 8-11 mice per group; scale bar, 50 μm and 100 μm
1067 (inset)) with corresponding **(L)** quantification of newborn neurons ($BrdU^+$ $NeuN^+$ cells) in the DG
1068 of WT and TIMP2 KO mice. Data are represented as mean ± SEM. Student's *t*-test for two-group
1069 comparisons. $^*P<0.05$; $^{**}P<0.01$; $^{***}P<0.001$. Data points represent individual mice. IHC,
1070 immunohistochemistry; DG, dentate gyrus; DCX, doublecortin.

1071

1072 **Figure 3.**

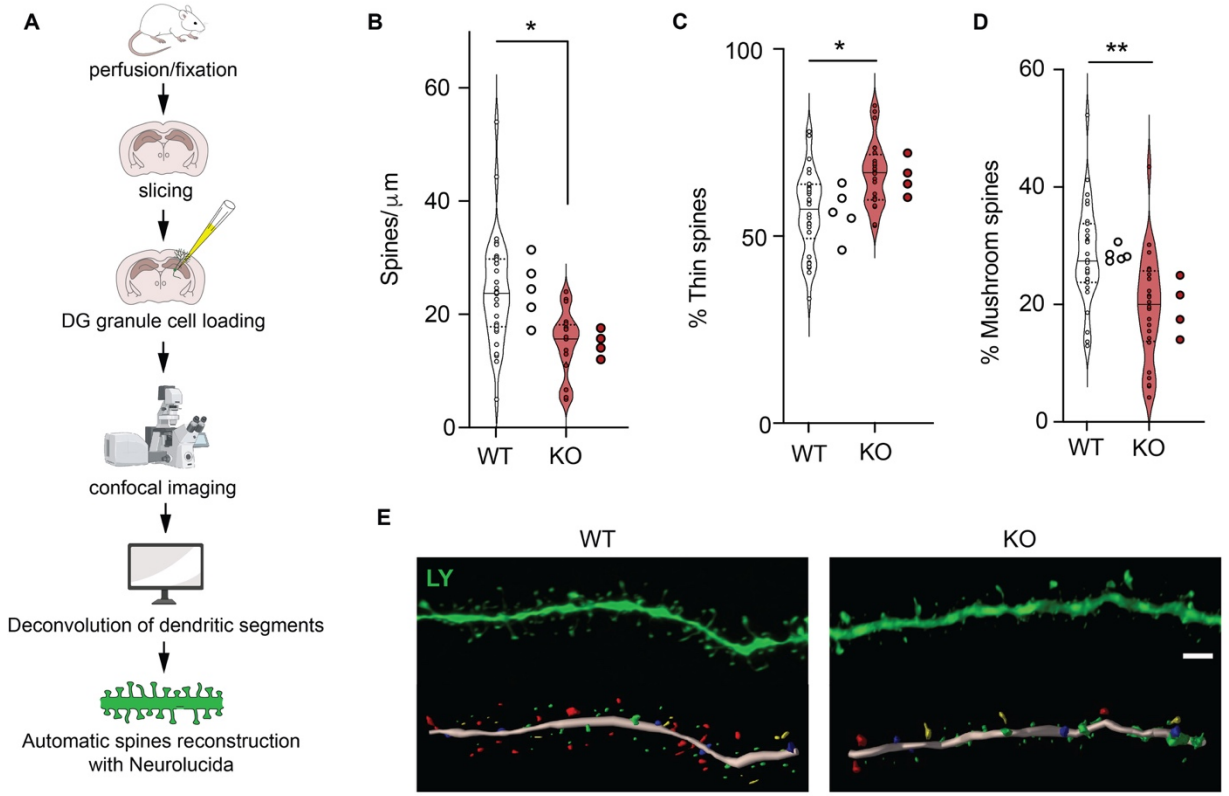

1073

1074 **Figure 3. TIMP2 regulates dendritic spine plasticity within the dentate gyrus.**

1075 **(A)** Schematic representation of the workflow for dendritic spine quantification using Lucifer
1076 Yellow-filled DG granule cells. **(B)** Overall dendritic spine density in DG granule cells
1077 iontophoretically labeled with Lucifer Yellow using sections isolated from six-month-old WT and
1078 TIMP2 KO mice (N=6 neurons per mouse from N=4-5 mice per group). **(C)** Quantification of the
1079 percentage of spines categorized according to "thin" spine heads or **(D)** "mushroom" spine heads.
1080 **(E)** Representative deconvolved confocal image of a dendritic segment from WT and TIMP2 KO
1081 Lucifer Yellow-labeled brain sections, and the downstream 3D reconstruction, with dendritic
1082 segment shown in pink, thin spines in green, stubby in blue, mushroom in red, and filopodia in
1083 yellow. Scale bar, 2 μm. Data are represented as mean ± SEM. Nested t-test for comparisons
1084 with neuron and mouse as levels. *P<0.05; **P<0.01. Data points represent neurons (left) and
1085 mice (right) for each group. LY, Lucifer Yellow.

1086

1087 **Figure 4.**

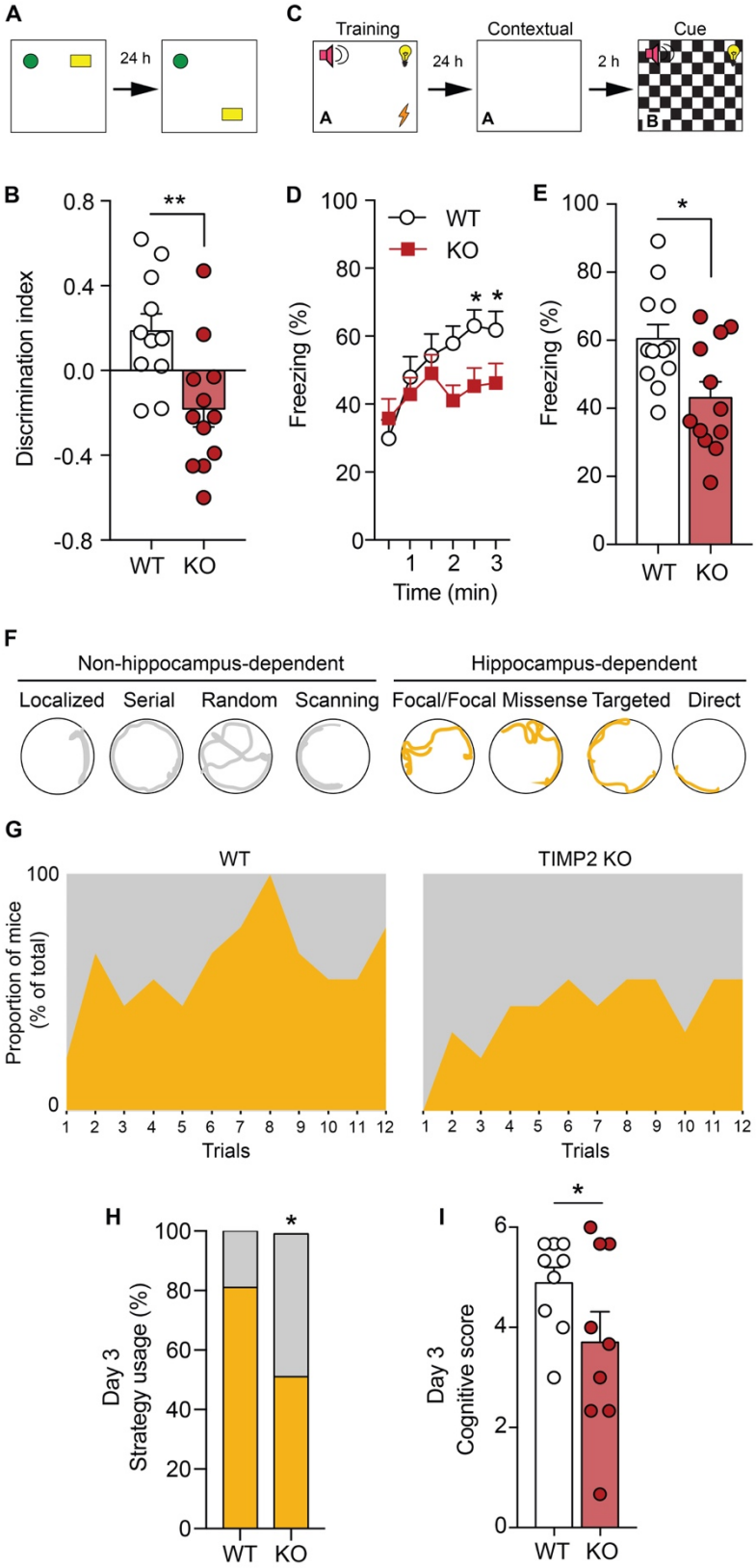

1090 **Figure 4. TIMP2 is required for hippocampus-dependent memory function.**

1091 **(A)** Schematic of the novel location recognition assay. **(B)** Discrimination index for novel location
1092 recognition on day 2 for WT and TIMP2 KO mice (2-3 months of age, N = 11-12 mice per group).
1093 **(C)** Schematic of the contextual and cued fear-conditioning assay. **(D, E)** Freezing levels by
1094 interval and overall measured in the conditioned-fear context A in WT and TIMP2 KO mice (2-3
1095 months of age, N = 11-12 mice per group). **(F)** Schematic diagram of modified Barnes maze with
1096 color coding for overall strategy classification. **(G)** Proportion of WT and TIMP2 KO mice using
1097 non-hippocampus-dependent (gray) and hippocampus-dependent (yellow) strategies during the
1098 testing trials (2-3 months of age, n = 9 mice per group). **(H)** Strategy utilization by WT and TIMP2
1099 KO mice on day 3 of the Barnes Maze and corresponding **(I)** cognitive scores, ranked by strategy
1100 complexity for WT and TIMP2 KO mice on day 3 in the Barnes Maze. Data are represented as
1101 mean ± SEM. Student's t-test for two-group comparisons in **(B, D, E)**, chi-square test in **(H)**, and
1102 nested t-test **(I)** for trial and mouse levels. *P<0.05, **P<0.01. Data points represent individual
1103 mice.

1104

1105 **Figure 5.**
1106

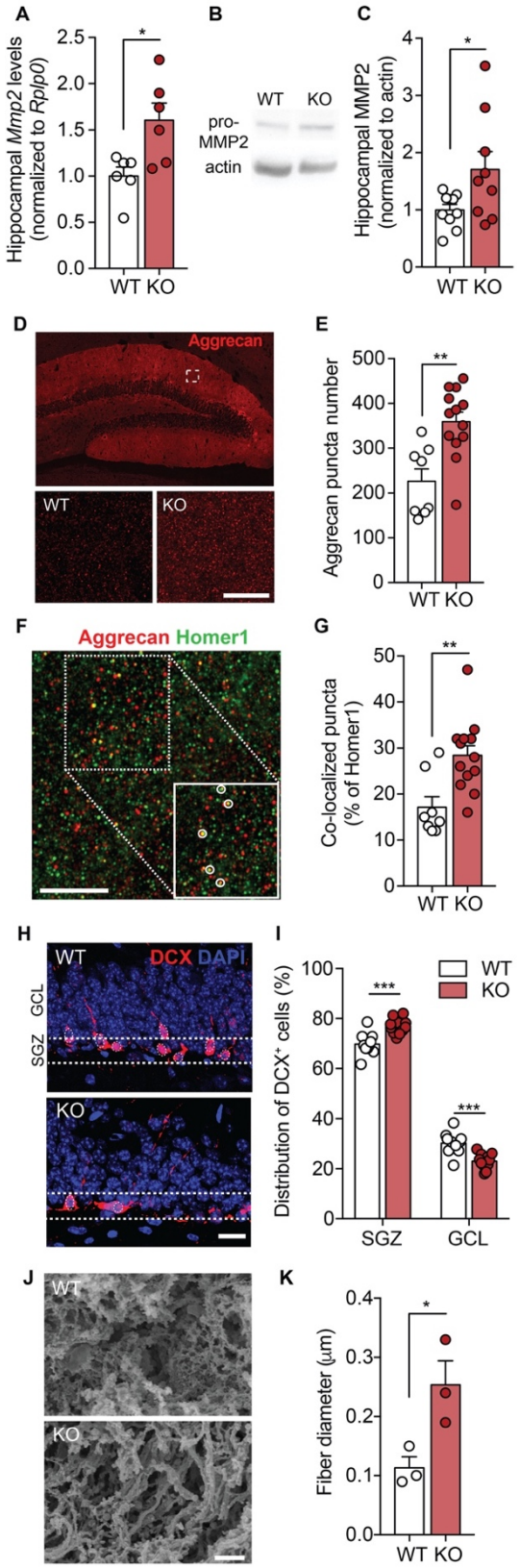

1107 **Figure 5. TIMP2 ablation leads to accumulation of ECM within the hippocampus.**

1108 **(A)** *MMP2* mRNA levels by qPCR from isolated hippocampus of WT and TIMP2 KO mice (2-3
1109 months of age, N = 6 mice per group). **(B)** Immunoblotting of MMP2 from hippocampal lysates of
1110 WT and TIMP2 KO mice (2-3 months of age, N = 9 mice per group) with corresponding **(C)**
1111 quantification of MMP2 protein levels. **(D)** Representative confocal microscopy images showing
1112 aggrecan puncta in the molecular layer of DG from WT and TIMP2 KO mice (2-3 months of age,
1113 N = 8-13 mice per group; scale bar, 5 μm) with corresponding **(E)** quantification of puncta. **(F)**
1114 Representative confocal microscopy images and corresponding **(G)** quantification of aggrecan
1115 and homer1 co-localization in the molecular layer of DG from WT and TIMP2 KO mice (2-3 months
1116 of age, N = 8-13 mice per group; scale bar, 5 μm). Circles indicate colocalized puncta. **(H)**
1117 Representative images showing the migration of DCX^+ cells in the SGZ and GCL of WT and
1118 TIMP2 KO mice (2-3 months of age, N = 11-12 mice per group, scale bar, 20 μm with
1119 corresponding **(I)** quantification of DCX^+ cells distributed in the subgranular zone (SGZ) and
1120 granule cell layer (GCL) of DG. **(J)** Representative surface scanning electron microscopy (SEM)
1121 from DG of WT and TIMP2 KO mice (2-3 months of age, N = 3 mice per group, scale bar, 2 μm,
1122 with corresponding **(K)** quantification of ECM microarchitecture in terms of fiber diameter
1123 measurements. Data are represented as mean ± SEM. Student's t-test for two-group
1124 comparisons. *P<0.05, ** P<0.01, ***P<0.001. Data points represent individual mice.

1125

1126 **Figure 6.**

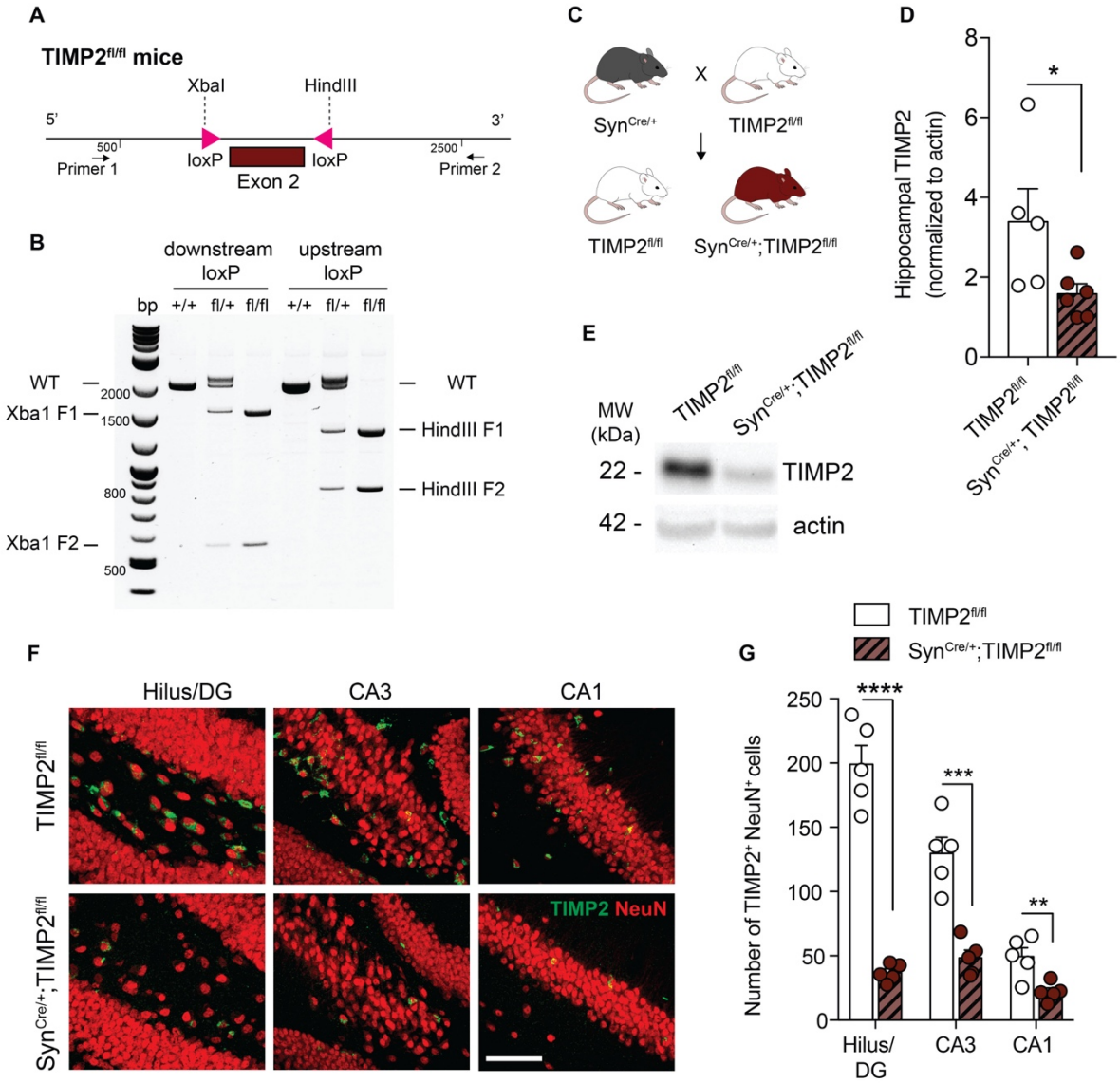

1127

1128 **Figure 6. Creation of a conditional model to target neuronal pools of TIMP2.**

1129 **(A)** Schematic illustration of the targeting strategy of to insert loxP sites flanking exon 2 to
1130 generate a model for conditional deletion of *TIMP2*. **(B)** Representative genotyping results
1131 revealing the PCR products for the mutant LoxP and wild-type alleles. Wild-type (+/+),
1132 heterozygous (fl/+), and homozygous (fl/fl) mice were identified according to this strategy. **(C)**
1133 Schematic diagram of cross-breeding strategy to establish neuron-specific TIMP2 deletion: male
1134 $TIMP2^{fl/fl}$ mice were mated with $Syn^{Cre/+}$ females to obtain $Syn^{Cre/+}$; $TIMP2^{fl/fl}$ and their respective
1135 $TIMP2^{fl/fl}$ littermate controls. **(D-E)** Representative TIMP2 immunoblot and corresponding
1136 quantification of TIMP2 protein levels from hippocampal lysate of $TIMP2^{fl/fl}$ and $Syn^{Cre/+}$; $TIMP2^{fl/fl}$
1137 (2-3 months of age, N = 5-6 mice per group). **(F)** High-magnification view of hilus/DG, CA3, and
1138 CA1 sub-regions of TIMP2+ cells co-expressing NeuN in $TIMP2^{fl/fl}$ and $Syn^{Cre/+}$; $TIMP2^{fl/fl}$ mice (2-
1139 3 months of age, N = 5 mice per group, scale bar, 20 μm) with corresponding **(G)** quantification
1140 of the total number of TIMP2+ cells with NeuN+ nuclei across hippocampal subregions. Data are
1141 represented as mean ± SEM. Student's t-test for two-group comparisons. *P<0.05, **P<0.01,
1142 ***P<0.001, ****P<0.0001. Data points represent individual mice.

1143

1144 **Figure 7.**

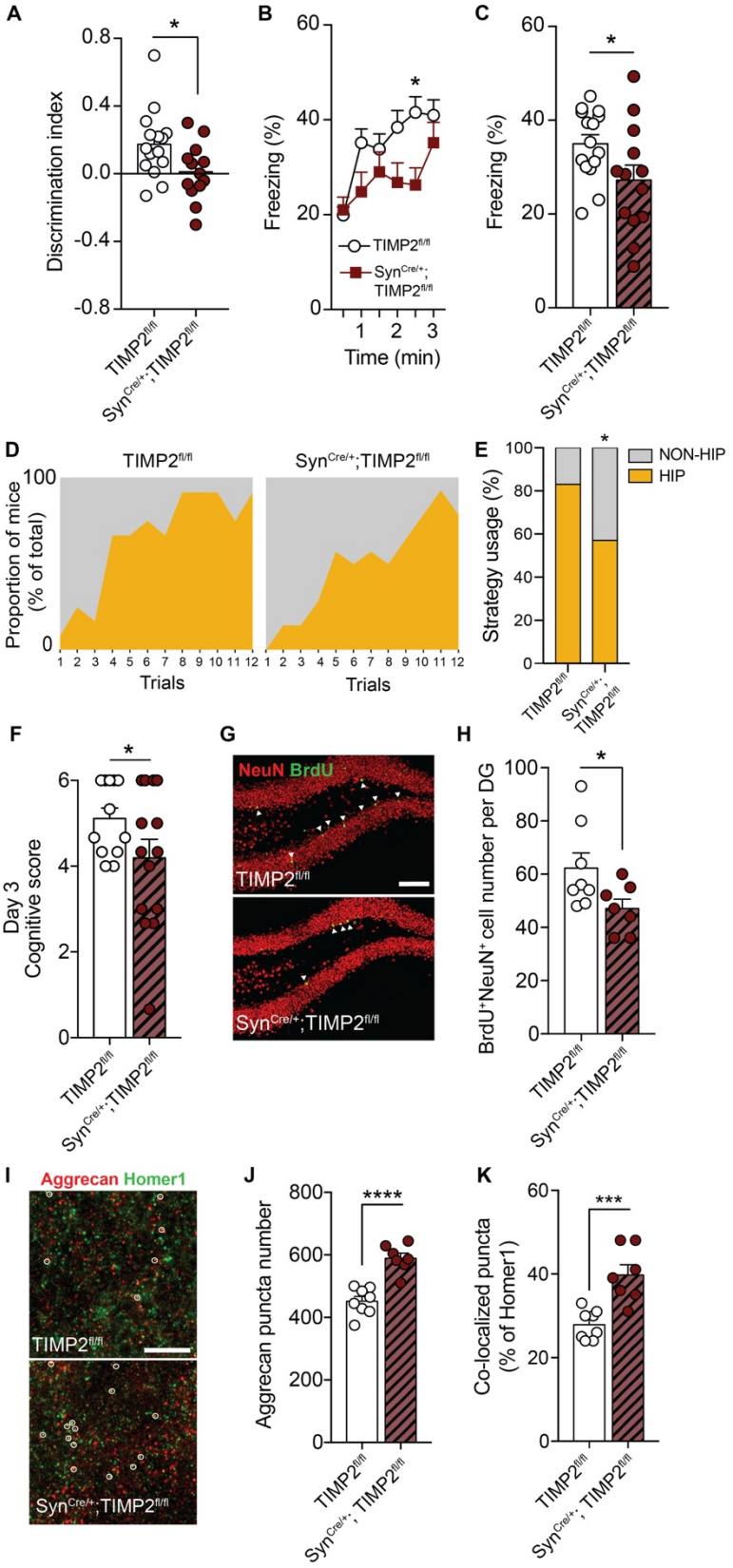

1146 **Figure 7. Neuronal TIMP2 regulation of the extracellular matrix regulates hippocampus-**
1147 **dependent cognitive function and adult neurogenesis.**
1148 **(A)** Discrimination index for novel location recognition on day 2 and **(B,C)** contextual fear-
1149 conditioning freezing levels in $TIMP2^{fl/fl}$ and $Syn^{Cre/+}$; $TIMP2^{fl/fl}$ mice (2-3 months of age, N = 13-
1150 15 mice per group). **(D)** Proportion of mice of each genotype using non-hippocampus-dependent
1151 (gray) and hippocampus-dependent (yellow) search strategies during the testing trials of $TIMP2^{fl/fl}$
1152 and $Syn^{Cre/+}$; $TIMP2^{fl/fl}$ mice in Barnes maze (2-3 months of age, N = 12-14 mice per group) with
1153 **(E)** quantification of the percentage of mice using these strategies by on day 3. **(F)** Cognitive
1154 complexity scores for $TIMP2^{fl/fl}$ and $Syn^{Cre/+}$; $TIMP2^{fl/fl}$ mice based on strategies used on day 3 of
1155 Barnes maze. **(G)** Representative confocal microscopy images of $BrdU^+$ and $NeuN^+$ cells in DG
1156 of $TIMP2^{fl/fl}$ and $Syn^{Cre/+}$; $TIMP2^{fl/fl}$ mice (2-3 months of age, N = 7–8 mice per group, scale bar,
1157 100 μm) with corresponding **(H)** quantification of $BrdU^+$ $NeuN^+$ newborn neurons in the DG. **(I)**
1158 Representative confocal microscopy images of aggrecan and homer1 puncta in molecular layer
1159 of DG of $TIMP2^{fl/fl}$ and $Syn^{Cre/+}$; $TIMP2^{fl/fl}$ mice (N = 7-8 mice per group, scale bar, 5 μm) with
1160 corresponding **(J)** quantification of aggrecan puncta and **(K)** co-localized puncta of aggrecan and
1161 homer1, as indicated by overlaid circles. Data are represented as mean ± SEM. Student's *t*-test
1162 for two-group comparisons in **(A-C)**, **(H)**, and **(J, K)**, chi-square test in **(E)**, and nested t-test **(F)**
1163 with trial and mice as levels. *P<0.05, ** P<0.01, ***P<0.001, ****P<0.0001. Data points represent
1164 individual mice.
1165

1166 **Figure S1.**
1167

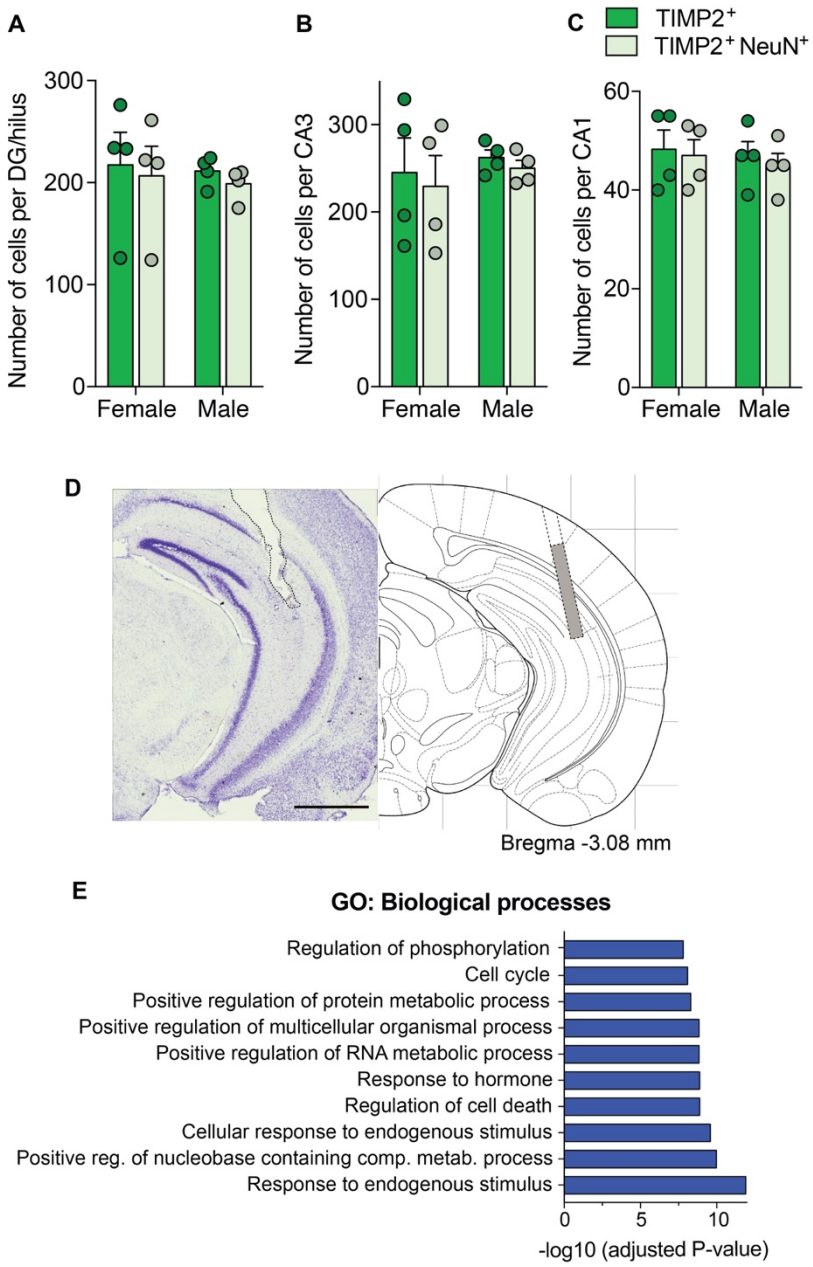

1168 **Figure S1. TIMP2 protein is found in hippocampal neurons in male and female mice, and**
1169 **its loss affects hippocampal transcriptome.**
1170 **(A)** Quantification of the total number of TIMP2$^+$ and TIMP2$^+$ NeuN$^+$ cells at the hilus/DG, **(B)** CA3
1171 and **(C)** CA1 subregions of the hippocampus from WT males and females at 2 months of age (N
1172 = 4 mice per sex). **(D)** Cresyl violet-stained section depicting the microdialysis probe tract through
1173 brain surface extending into hippocampus, with microdialysis probe position seen at Bregma -
1174 3.08mm based on Paxinos and Watson atlas. Scale bar, 500 μm. **(E)** Top 10 significant pathways
1175 for upregulated DEGs in hippocampi of TIMP2 KO mice relative to WT mice (N = 13-17 mice per
1176 group). Data are represented as mean ± SEM.
1177

1178 **Figure S2.**

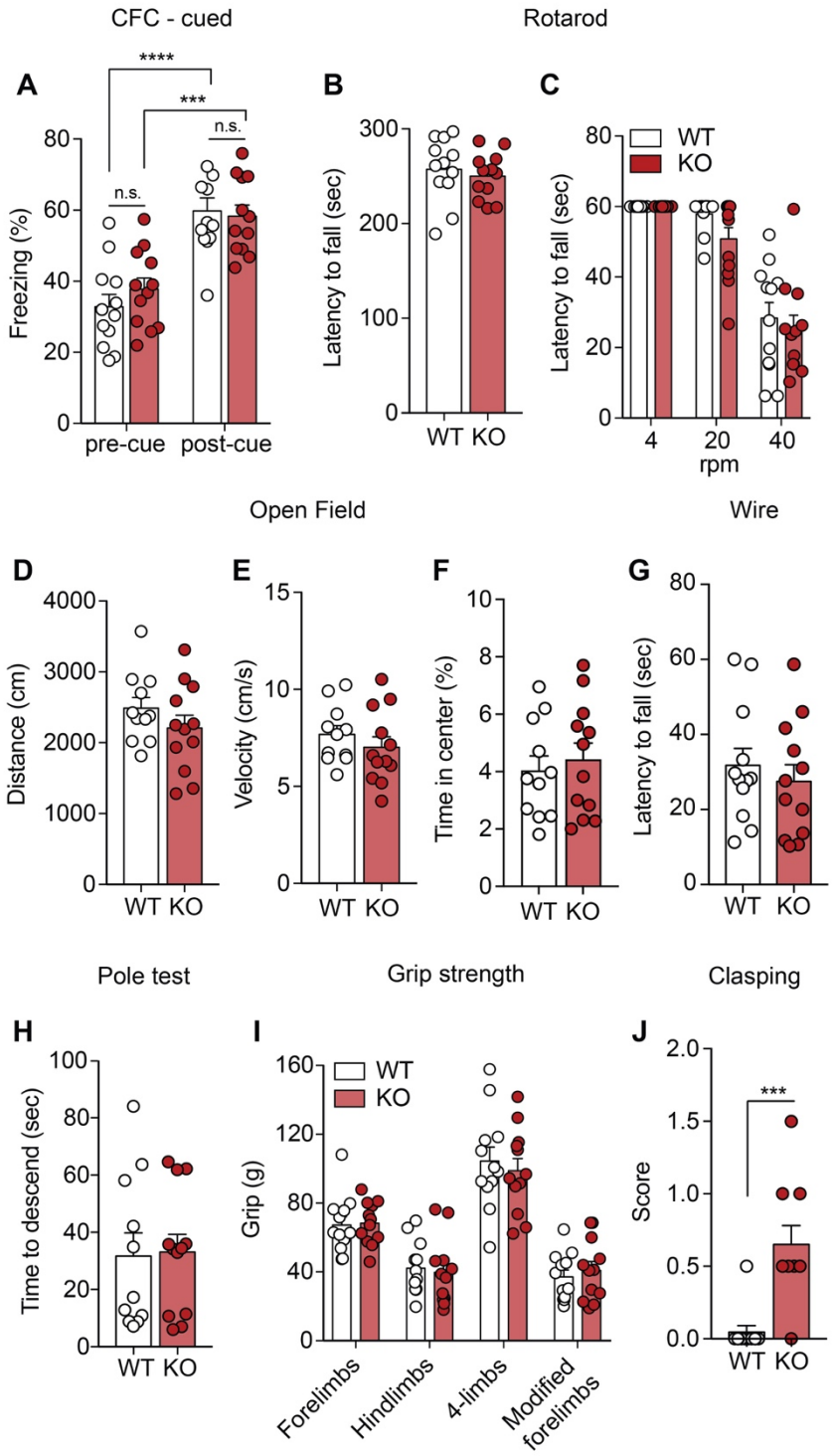

1181 **Figure S2. Loss of TIMP2 does not affect amygdala-associated behavior or overall motor**
1182 **function**

1183 **(A)** Percentage of freezing detected in the cued task of the fear-conditioning assay in WT and
1184 TIMP2 KO mice (2-3 months of age, N = 12 mice per group). **(B)** Latency of TIMP2 KO and WT
1185 mice to fall in the rotarod in the fixed and **(C)** acceleration protocol at 4, 20 and 40 rpm (N = 12
1186 mice per group). **(D)** Total distance traveled by TIMP2 KO and WT mice in the open field, as well
1187 as **(E)** velocity, and **(F)** percentage of time spent in the center of the arena (N = 11-12 mice per
1188 group). **(G)** Latency of TIMP2 KO and WT mice to fall in the wire test (N = 12 mice per group). **(H)**
1189 Time for TIMP2 KO and WT mice to descend the pole in the pole test (N = 11-12 mice per group).
1190 **(I)** Grip strength of the fore-, hind- and four limbs in TIMP2 KO and WT mice (N = 12 mice per
1191 group). **(J)** Hindlimb extension by clasping score in TIMP2 KO and WT mice (N = 10-11 mice per
1192 group). Data are represented as mean ± SEM. Student's *t*-test for two-group comparisons. n.s.,
1193 not significant.

1194

1195 **Figure S3.**

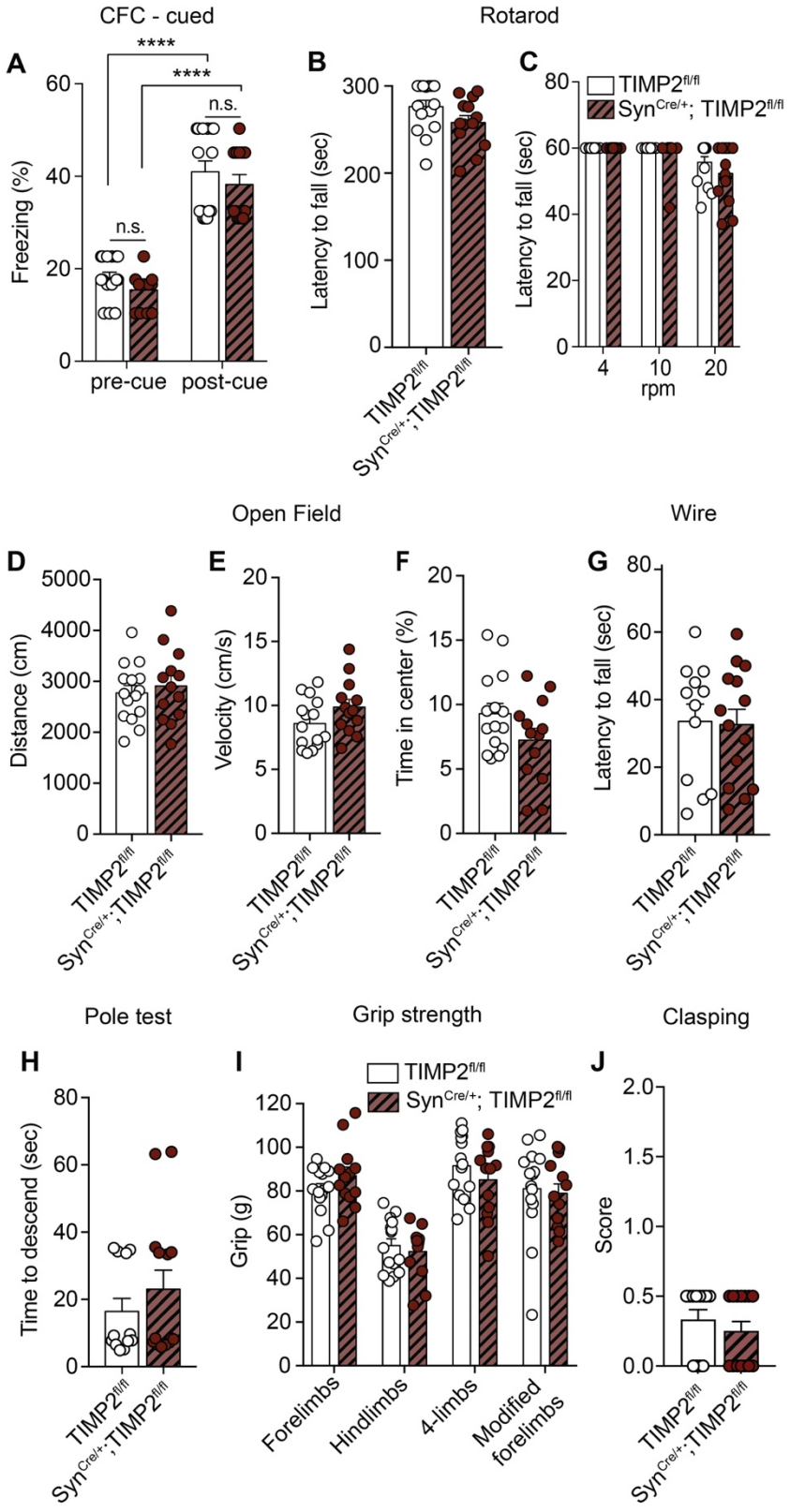

1198 **Figure S3. Neuronal TIMP2 deletion does not impair amygdala-associated behavior or**
1199 **overall motor function**

1200 **(A)** Percentage of freezing detected in the cued task of the fear-conditioning assay in $TIMP2^{fl/fl}$
1201 and $Syn^{Cre/+}$; $TIMP2^{fl/fl}$ mice (2-3 months of age, N = 13-15 mice per group). **(B)** Latency of
1202 $TIMP2^{fl/fl}$ and $Syn^{Cre/+}$; $TIMP2^{fl/fl}$ mice to fall in the rotarod in the fixed and **(C)** acceleration protocol
1203 at 4, 10 and 20 rpm (N = 13-15 mice per group). **(D)** Total distance traveled by $TIMP2^{fl/fl}$ and
1204 $Syn^{Cre/+}$; $TIMP2^{fl/fl}$ mice in the open field, as well as **(E)** velocity, and **(F)** percentage of time spent
1205 in the center of the arena (N = 13-15 mice per group). **(G)** Latency of $TIMP2^{fl/fl}$ and $Syn^{Cre/+}$;
1206 $TIMP2^{fl/fl}$ mice to fall in the wire test (N = 12-14 mice per group). **(H)** Time for $TIMP2^{fl/fl}$ and $Syn^{Cre/+}$;
1207 $TIMP2^{fl/fl}$ mice to descend the pole in the pole test (N = 12-14 mice per group). **(I)** Grip strength of
1208 the fore-, hind- and four limbs in $TIMP2^{fl/fl}$ and $Syn^{Cre/+}$; $TIMP2^{fl/fl}$ mice (N = 13-15 mice per group).
1209 **(J)** Hindlimb extension by clasping score in $TIMP2^{fl/fl}$ and $Syn^{Cre/+}$; $TIMP2^{fl/fl}$ mice (N = 12-14 mice
1210 per group). Data are represented as mean ± SEM. Student's *t*-test for two-group comparisons.
1211 n.s., not significant.